LBL-11436

Nuclear States and Shapes at High Spin*

R. M. Diamond
Lawrence Berkeley Laboratory
University of California
Berkeley, California 94720 U.S.A.

DISCLAIMER

This [illegible] prepared as an account of work spon[illegible] United States Government nor any agen[illegible] warranty, express or implied, or assumes any le[illegible] completeness, or usefulness of any information [illegible] apparatus, product, or process disclosed, [illegible] would not infringe privately [illegible] process or service by trade name [illegible] not necessarily constitute or imply its endorsement [illegible] States Government or any agency thereof. The views a[illegible] necessarily state or reflect those of the United States Gov[illegible] agency of the United States Government [illegible] nor any of their employees, makes any [illegible] or responsibility for the accuracy, [illegible] product, or process disclosed, [illegible] rights. Reference herein to any specific [illegible] manufacture, or otherwise does [illegible] endorsement, or favoring by the United [illegible] and opinions expressed herein do not [illegible] any agency thereof.

*This work was supported by the Division of Nuclear Physics of the Office of High Energy and Nuclear Physics of the U.S. Department of Energy under Contract W-7405-ENG-48.

DISTRIBUTION OF THIS DOCUMENT IS UNLIMITED

Abstract

As angular momentum is added to a nucleus, the balance of forces acting upon it to determine its shape, moment of inertia, mode of rotation, and type of level structure may undergo a series of changes. At relatively low spins a deformed nucleus will rotate collectively, and one may see the effect of Coriolis anti-pairing in gradually increasing the moment of inertia. Around spin 12-16 $\hbar$ there may be an abrupt change (backbending) when a pair of high-j nucleons unpair and align with the axis of rotation, thus allowing the nucleus to slow its collective rotation. This process, the start of a sharing of angular momentum between single-particle motion and the collective rotation, gives a lower total energy and corresponds to a change towards triaxiality in the shape of the nucleus. At much higher spins we can no longer observe discrete γ-ray transitions, but are in the regime of continuum spectra; all the information on these high-spin states (to 65 $\hbar$) is contained in these continuum cascades. We are beginning to learn how to study these spectra, experimentally and theoretically, and new techniques offer promise of letting us extract a great deal of information about the shapes and properties of very high spin states.

I want to discuss with you what happens when a nucleus takes on more and more angular momentum. What are the changes in its shape, its properties, its level structure? For a non-spherical nucleus, one of the simplest modes of excitation upon receiving a few units of angular momentum is rotation as a whole. This motion has some similarities with the rotation of a macroscopic object; in favorable cases the energy levels and transition energies of an even-even nucleus follow the pattern of a rigid rotor,

$$E = \frac{\hbar^2}{2\mathcal{J}} I(I + 1) \quad , \tag{1}$$

$$E_\gamma = \frac{\hbar^2}{2\mathcal{J}} (4I - 2) \quad . \tag{2}$$

The transition probabilities between these levels are strongly enhanced over single-particle values and depend upon an intrinsic quadrupole moment, Q_0, and geometric factors, the Clebsch-Gordan coefficients

$$B(E2;I_iK \rightarrow I_fK) = \frac{5}{16\pi} e^2 Q_0^2 \langle I_i K 20 | I_f K \rangle \quad . \tag{3}$$

Such rotation of deformed nuclei was first proposed by A. Bohr[1], and now there are many examples of this behavior. Figure 1 shows the spectrum from ^{174}Yb Coulomb excited with a ^{136}Xe beam[2]; the transitions of the ground-state rotational band are seen up to the $20^+ \rightarrow 18^+$ transition, and the nearly evenly spaced lines follow Eq. (2) rather well. Another example is the spectrum from ^{238}U Coulomb excited by ^{208}Pb to the 28^+ level[3], Fig. 2. Plotting the ratio $B(E2;I \rightarrow I - 2)_{exp}/B(E2;I \rightarrow I - 2)_{rotor}$ removes the coefficients in Eq. (3) and shows the variation of

Q_0 as a function of spin; Fig. 3 gives this ratio for ^{232}Th (ref. 4). It can be seen that the model holds with a constant Q_0 within the experimental accuracy.

However, it was early recognized that the experimental moments of inertia, $\mathcal{J}$, determined from Eqs. (1) and (2) were only one-half to one-third the rigid-rotor value. This discrepancy was due to the neglect of the residual interactions between the nucleons, in particular, of the pairing correlations[5]. These correlations introduce irrotational components into the matter flow pattern of nuclei and thus reduce the value of $\mathcal{J}$[6,7]. It was expected that as angular momentum was added to a nucleus, the pairing correlations would be quenched and finally disappear, and in the process $\mathcal{J}$ would rise to the rigid-rotor value. Such a gradual increase in $\mathcal{J}$ with spin is, in fact, observed (Coriolis anti-pairing) and constitutes a general type of deviation from Eq. (1). It is often well accounted for by the VMI[8] or Harris[9] expressions for the energy.

A more exciting type of deviation from Eqs. (1) and (2) was discovered some years ago[10] when it was found that in several rare-earth nuclei at spins between 12 and 18 $\hbar$ the γ-ray transition energy did not continue to increase regularly with spin but actually abruptly decreased (backbent) before starting up again. On a plot of excitation energy, E*, vs spin, I, this is hardly noticeable, as shown in Fig. 4 for ^{164}Yb (ref. 11), but in the conventional plot of $2\mathcal{J}/\hbar^2$ vs $(\hbar\omega)^2$ (insert in figure) the effect is very striking. Actually since the γ-ray energies are what are directly measured experimentally, the

decrease in transition energy is a very noticeable change in behavior. The most well-studied region illustrating this phenomenon of backbending is that of the rare-earth nuclei shown in Fig. 5, each section of which is a plot similar to the insert in Fig. 4. It is clear that the light rare-earth region has strong backbenders, as does the region around Os. However, the neutron-rich nuclei in the middle of the region seem to backbend much less, if at all. It seems that the effect can show considerable variation fromn nucleus to nucleus even within a region.

It is now generally agreed that the usual origin of this phenomenon[12] is a crossing of the ground band by an excited band with a larger effective $\mathcal{J}$. This can be seen in the case of ^{164}Er, where levels of both bands are known both above and below the crossing[13,14]. The decay scheme is shown in Fig. 6, and a plot of the level energies vs spin is given in the lower part of Fig. 7. The ground band is crossed between spins 14 $\hbar$ and 16 $\hbar$ by the band labeled "yrast even", and this is shown on the left side of the backbending plot, Fig. 8. Individually the bands yield reasonably smooth lines. However, the yrast levels switch at spin 14 $\hbar$ from the ground band to the yrast-even band, using one interband transition. This sequence forms the usual backbend, which is now seen to result from pieces of two different bands. At the crossing point there is an interaction between the bands which perturbs a few of the levels. This causes some scatter in the level energies at just this point, as can be seen in the solid points in Fig. 8. A constant interaction matrix element of 45 keV between levels in the two bands

results in unperturbed level positions given by the open circles. These are quite smooth. The E2 branching ratios can also give a value for the mixing and thus the interaction matrix elements. This analysis gives 50 keV, in excellent agreement with the value from the energies.

The right side of Fig. 8 shows the backbending plot for the γ band in ^{164}Er. The odd-spin members are smooth up to spin 13$\hbar$, where the backbend occurs. The even-spin members, however, show a perturbation at spin 10$\hbar$. A shift of 25 keV in the 10^+ member of this band (open circles) just removes this perturbation and is what one might expect from the intersection with the yrast-even band, although its 10^+ member has not been observed. The absence of a similar effect in the odd-spin members is good evidence that the yrast-even band has no such states (hence the name). The fact that the bands may have only even or odd spins is an expected result of strong Coriolis interaction at high rotational frequencies. The backbend around spin 14$\hbar$ for the γ band occurs in both the even- and odd-spin states showing the presence of both of these in the crossing bands (yrast odd and yrare even). This entire behavior is very well reproduced in simple calculations[15], as shown in the top part of Fig. 7. In this interpretation the two upper bands, together with the yrast-even band, are all two-quasiparticle states based on two $i_{13/2}$ neutrons whose angular momentum has been largely aligned along the rotation axis. Finally the yrare-even band in Fig. 7 seems likely to intersect the ground band at the highest spins observed (22$\hbar$), and this probably causes the upbend in

this band, shown in Fig. 8. This nucleus is one of the most favorable for observing backbending behavior, though there are some other excellent examples. It is clear that backbending is the result of a band crossing, and the interesting question then has to do with the nature of the crossing band.

Strong clues as to what kind of two-quasiparticle band is involved is provided by "blocking" experiments[16]. The idea behind such experiments is that one studies a band in an odd-mass nucleus where the odd particle occupies some particular orbital, say an $i_{13/2}$ neutron orbital. If, then, the crossing band involves this $i_{13/2}$ neutron as one of its components, the crossing will not occur in the odd-mass nucleus since that orbital is already occupied and not available. Exactly this is seen to occur in Fig. 9, where the $i_{13/2}$ band in ^{157}Er is plotted together with the ground bands of both ^{156}Er and ^{158}Er (ref. 16). Whereas the even-even nuclei backbend at $(\hbar\omega)^2) \approx 0.08$, the $i_{13/2}$ band in ^{157}Er clearly does not. This is evidence that this particulr orbital is indeed involved in the crossing band. The $h_{11/2}$ proton orbital can also be tested by studying this band in odd-mass Ho nuclei. Figure 10 shows the data[17] which indicate clearly that the $h_{11/2}$ band <u>does</u> backbend like the adjacent even-even nuclei and is therefore <u>not</u> involved in the crossing band. Many tests of this type have shown the crossing band to be composed of two aligned $i_{13/2}$ neutrons in the light rare-earth region. In the heavier region (around Os) this may also be the case, but that is not so clear yet.

A second backbend has been observed in the yrast sequence of a few nuclei[18,19]. In Fig. 11 data for ^{158}Er are shown, together with the level scheme of this nucleus above spin 22 $\hbar$. The corresponding backbending plot is shown in Fig. 12, where the usual backbend is seen around $(\hbar\omega)^2 \approx 0.08$, and in addition an upbend at $(\hbar\omega)^2 \approx 0.18$ occurs. This upbend indicates another band crossing, whose origin is not clear since the appropriate blocking experiments are difficult to do at such high spins. Calculations suggest this (second) pair of quasiparticles correspond to aligned $h_{11/2}$ protons.

Thus, an experimental spectroscopy of backbends is emerging, and there are simultaneous developments in theory. A modified harmonic oscillator potential (MHO), the Nilsson potential[20], has been very successful in representing the average potential generated by the nucleons in order to calculate the individual nucleon energy levels as a function of deformation. For large deformation, Strutinsky devised a smearing procedure to normalize the average behavior to that of the liquid-drop model[21]. It has been reasonably straightforward to "crank" this potential around the x axis by adding a term $-\omega j_x$, and calculate the orbits in a potential rotating with frequency ω[22-25]. A variation to this approach is to use a Wood-Saxon (WS) potential[26]. This removes some problems in the average moment of inertia having to do with the ℓ^2 term in the MHO potential, but on the whole seems to give very similar results. The Hartree-Fock (HF) potential, where self consistency between the potential and calculated orbits is required, has also been used, and pairing has been included in the Hartree-Fock-Bogulubov (HFB) method[27-29].

In the spherical shell model there is a $(2j + 1)$ degeneracy of levels in a j-shell, which is largely lifted by deforming the potential. The resulting levels are two-fold degenerate corresponding to time reversal symmetry of the nucleon motion and are characterized by their projection on the symmetry axis, Ω. If a given deformation, say $\epsilon = 0.2$, is chosen, the resulting system can be cranked, and Fig. 13 shows some of the levels from a Nilsson diagram[24] at $\epsilon = 0.2$ as a function of cranking frequency ω, given in units of the oscillator frequency, ω_0. The energy $e'(\omega)$ is in the rotating frame and in units of $\hbar\omega_0$.

$$\hbar\omega_0 = 41/A^{1/3} \text{ MeV} \quad . \tag{4}$$

The time reversal degeneracy of the levels is lifted, and the slope of these levels $de'(\omega)/d\omega$ is proportional to the aligned angular momentum. The strongly aligned high-j orbits are the steeply down-sloping ones, with a limiting slope corresponding to their maximal alignment. Figure 14 is a diagram of this same type[19,30], except that pairing is included, and it covers only a very restricted region, the five states nearest the Fermi level for neutrons around $N = 90$. The $e'(\omega) = 0$ line is the Fermi level, and each state is reflected around this line, so that it appears twice. A rough way to think about this is that in one case [$e'(\omega) < 0$ for low ω] the level is included in the pairing correlations, and in the other [$e'(\omega) > 0$ for low ω] it is not included, so that it is a quasiparticle. If particles are placed in the levels labeled A and B (thereby necessarily emptying those labeled -A and -B), a

two-quasiparticle excited band is formed which corresponds (at $\omega > 0.02$) to the most-aligned $i_{13/2}$ components. As the frequency increases, the energy of this band drops relative to the fully paired vacuum ($e' = 0$) until at the point labeled ω_1 it crosses the vacuum and becomes lowest in energy. This crossing corresponds to the first backbend and has been observed in many nuclei. If one follows only the lowest band, then this process may be expressed as AB unpairing (or aligning) at frequency ω_1. The important point is that AB will unpair in essentially <u>every</u> excited band at this frequency. For example, the two-quasiparticle band EF will be crossed by the four-quasiparticle band ABEF, again at ω_1, and for EF one could substitute CD, or CDEF, etc. The value of $\hbar\omega$ is a measurable quantity ($\sim E_\gamma/2$), and the above argument says that at certain transition energies many bands at widely different excitation energies will experience a backbending (band crossing). However, a complication occurs if state A has a quasiparticle in it (either a single one in an odd-mass nucleus or one of a pair such as AE in an even-even nucleus). Then AB cannot unpair--A is blocked--and this backbending will not occur. The frequency then increases normally with spin to about $\hbar\omega = 0.36$ MeV, the point marked ω_2, where BC will unpair and align. Again this band crossing can happen in many bands. It is worth noting that at about this same frequency--0.36 MeV--AD unpairs, so that if B rather than A is blocked, then AD can unpair and cause a band crossing.

The experimental data[19] that support such a picture are shown in Fig. 15. Here the aligned angular momentum i is plotted vs $\hbar\omega$. The aligned angular momentum is obtained from the experimental data by subtracting the spin of the ground band (no quasiparticles) from the spin of the band of interest <u>at the same rotational frequency</u> (transition energy). The upbends or backbends in Fig. 15 correspond to band crossings, and the sharp backbend in the ground band at $\hbar\omega_1 \sim 0.27$ MeV is in reasonable agreement with the AB unpairing energy of 0.23 MeV in Fig. 14. The remarkable feature of Fig. 15 is the coincident upbending of six bands at frequencies around ω_2, 0.36 MeV. These include three bands where A is blocked (AE and AF in ^{160}Yb and A itself in ^{161}Yb), two where B is blocked (BF in ^{160}Yb and B itself in ^{161}Yb), and the pairing vacuum as an excited band above the point where AB crossed. The yrast band has a second band crossing at frequency ω_3 (~0.42 MeV) which is probably due to a pair of $h_{11/2}$ protons and so is not shown in Fig. 14.

Some new features emerge from these considerations. Bands can be characterized by their signature (odd or even spin members) and their alignment, i, in addition to the usual properties, parity and excitation energies. Backbends can be characterized by the frequency, ω, at which they occur, the alignment change, Δi, and the amount of interaction between the bands. From these properties it should be possible to identify the observed features with those of calculations, e.g., Fig. 14. It will be very interesting to see how far one can develop such analyses of high-spin bands and backbends.

One important feature should be noted. In some nuclei by spin 20 $\hbar$ the purely collective ground-band states are no longer yrast; a two-quasiparticle aligned band lies lowest. Around spin 30 $\hbar$, a four-quasiparticle aligned band may cross and lie even lower. (This may be more general than appears at first sight; if the mixing matrix element between the crossing bands is sufficiently large, there is no backbend and the yrast curve is relatively regular, but the lowest band has still changed its nature.) The addition of angular momentum is converting the purely collective rotation of the nucleus as a whole into a mixture of collective and single-particle motions whose spin axes are parallel and thus optimally efficient in carrying the angular momentum. Since the orbits of the high-j aligned particles are roughly in the plane perpendicular to the rotation axis, this will cause an equatorial bulge in the initially prolate nucleus. Thus the nucleus will lose its axial symmetry and become somewhat triaxial. How far can, and does, this process continue as more particles align?

The previous discussion has taken us up in spin to ~30 $\hbar$. As you will see shortly, discrete states are known to ~38 $\hbar$. Is that the largest amount of spin a nucleus can hold, and, if not, what are the limits? The limitation on how much angular momentum a nucleus can hold is usually provided by its tendency to fission, to fall apart under centrifugal pressure. An estimate of the maximum spin before fission sets in can be obtained from the liquid-drop model. Figure 16 shows a plot (solid line) of angular momentum for which the fission barrier becomes zero vs

the mass number of the nucleus (along the valley of β stability) taken from ref. 31. Actually, nuclei still fission even with small fission barriers, so the dashed curve, representing the angular momentum limit for a barrier of 8 MeV, is more realistic. Below this curve, particle emission dominates the decay and is followed by a cascade of γ-ray transitions to remove the remaining excitation energy and spin. The dashed curve is still an upper limit to the angular momentum at the top of the γ cascades, as the particles can carry off a little spin, and in the case of α-particle emission (common for nuclei with $Z < 50$) a considerable amount of angular momentum may be removed. However, in the most favorable cases around $A = 135$, maximum spins of 60-70 $\hbar$ are still to be expected.

The shape, and a related quantity, the moment of inertia, $\mathcal{J}$, of a nucleus at high spin can also be considered in the light of the liquid-drop model. The moment of inertia depends on both the shape and the pattern of mass flow, but at higher spin (>30 $\hbar$) the pairing correlations are thought to be quenched, leading to rigid flow. The shape of a rigid ellipsoid can be expressed in terms of the parameters σ and γ, defined so that the semi-axes r_i are related to the mean radius R by $r_i = a_i R$ where

$$\begin{aligned} a_1 &= e^{\sigma} \cos(\gamma - 2\pi/3) \\ a_2 &= e^{\sigma} \cos(\gamma + 2\pi/3) \\ a_3 &= e^{\sigma} \cos \gamma \quad . \end{aligned} \tag{5}$$

At small deformation this gives $\Delta R/R \approx \epsilon \approx 1.5\sigma$ and $\beta \approx 1.6\sigma$. For such an ellipsoid,

$$\mathcal{J}_1 = \frac{1}{5}M(r_2^2 + r_3^2) = \frac{1}{2}(a_2^2 + a_3^2)\mathcal{J}_0 \tag{6}$$

where $\mathcal{J}_0$ is the rigid sphere value, and the axes may be permuted cyclically. Values of $\mathcal{J}_0$ can be obtained from the expression for a rigid sphere given by Myers[32],

$$\frac{2\mathcal{J}_0}{\hbar^2} = \frac{4MR_s^2}{5\hbar^2} = 0.01913\ A\ R_s^2(\mathrm{fm})\ \mathrm{MeV}^{-1} \tag{7}$$

with the equivalent sharp radius[33]

$$R_s = 1.28\ A^{1/3} - 0.76 + 0.8\ A^{-1/3}\ \mathrm{fm}\ . \tag{8}$$

Plots of $\mathcal{J}/\mathcal{J}_0$ vs γ for two values of the deformation parameter, $\varepsilon \approx 0.3$ and $\varepsilon \approx 0.6$ [$\sigma \approx 2/3(\varepsilon)$], are shown in Fig. 17. These values correspond to the usual well-deformed rare-earth nucleus and to the unusual nucleus with a 2:1 ratio of axes. The four limiting cases of axially symmetric ellipsoids, prolate or oblate, and rotating about an axis parallel or perpendicular to the symmetry axis, are shown explicitly. The scale on the right-hand side gives the change in rotational energy for a nucleus with A = 160 and I = 60 caused by the change in $\mathcal{J}$ from $\mathcal{J}_0$. It can be seen that the oblate shape rotating around its symmetry axis and the prolate shape rotating perpendicular to its symmetry axis have the lowest energies among the limiting cases by 10-20 MeV, and the triaxial region between them is relatively flat.

It is not, however, obvious that the full liquid-drop energy will follow this behavior, since there is also a shape dependence for both the surface and Coulomb energies which must be added. But their dependence on γ comes in only as a high-order term (third power in σ) which is small, so that the full liquid-drop energy at high spins does follow rather closely the

moment-of-inertia behavior shown in Fig. 17. In fact, the points along the $\varepsilon \approx 0.3$ curve have the Coulomb and surface shape energies added, and they come near the curve for the rotational energy alone. Thus the oblate shape rotating about the symmetry axis lies lowest in the range of deformation at which most nuclei occur, but the prolate ellipsoid rotating about an axis perpendicular to the symmetry axis and the triaxial nuclei in between lie at a not much higher energy. They are even lowest for $\sigma >$ 0.5. Actually, real rotating nuclei at moderate deformation can be prolate rather than oblate, due to shell effects, as will be discussed.

Shell effects are one of two additional factors that must be considered in going from liquid-drop to real nuclei. The other is that nuclei are small quantal systems; thus they cannot rotate collectively about a symmetry axis--there is no way to orient them with respect to such an axis. It was understood for some time that this meant these degrees of freedom were contained in the single-particle motion. However, when Bohr and Mottelson[34] considered aligning particle angular momenta along a symmetry axis, they realized that <u>on the average</u> the energy was the same as rotating the system classically about that axis. This was shown only in the Fermi gas approximation, but it is believed to be true, or approximately so, for a realistic nuclear system. The states of such a system have single-particle character and are irregular in energy, in contrast to rotation perpendicular to the symmetry axis which can be collective with smooth energies and strongly enhanced E2 transition probabilities.

Finally, the shell effects must be added. Nuclear levels in a potential well are grouped together into shells, as are electrons in an atom. Certain nucleon numbers ("magic numbers") complete shells and have extra stability in analogy to the noble gas electronic structures. However, when nuclei deform, the shells change, so that the number to complete a shell is different. Thus, in general, a given nucleon number will prefer that shape which makes it look most nearly like a closed shell. These shell effects can be as large as 10-12 MeV, (the double-closed spherical shell at ^{208}Pb), but on the average might be 3-4 MeV. At low spins, the shell effects are often larger than the rotational energy differences due to shape differences, and so determine the shape. At high spin the shell effects remain of the same order, but the differences in rotational energy with shape can reach 10-20 MeV (Fig. 17), so that here one expects only oblate shapes rotating around the symmetry axis (non-collective behavior with isomers) or prolate shapes rotating collectively (smooth bands and no isomers). Since these behaviors appear quite different experimentally, there is hope to learn about the shapes and dynamics of nuclei at these spin values.

Now let us consider what happens to nuclei when provided with the largest amount of angular momentum they can hold without fissioning. Why, even in the most favorable cases, are discrete states seen only to spins of 38 $\hbar$? For example, nuclei of mass ~150 produced in a heavy-ion compound nuclear reaction may have 70 $\hbar$ of spin. They initially evaporate nucleons, usually

neutrons, which remove energy but little spin until the excitation energy above the yrast line is of the order of a neutron binding energy or less. How many neutrons are so emitted to make the final product depends upon the initial spin and excitation energy of the compound nucleus, as the higher the spin, the higher the yrast energy and the smaller the amount of thermal energy available to emit neutrons. When the nucleus no longer has enough energy to emit another particle, then the remaining excitation energy and the angular momentum are carried off by γ-ray cascades. These involve several types of γ-ray transitions.

The nucleus can decay vertically toward the yrast line by statistical transitions that "cool" the nucleus, carrying off energy but little angular momentum, or by collective E2 transitions that form bands parallel to the yrast line and carry off two units of spin apiece as well as energy (Fig. 18). There are many pathways, so that no single transition has enough intensity to stand up in the spectrum; this leads to the name "continuum" γ-ray spectrum. When the nucleus cools to near the yrast line, then there are fewer pathways and enough population goes through the individual transitions to make them stand out in the spectrum as resolved lines and indicating discrete states. This happens between spins of $10\hbar$ to $40\hbar$ depending on the type of nucleus, and the observed lines can correspond to either collective or noncollective transitions, according to the nature of the yrast levels.

We believe that the statistical transitions do not depend very much on the nuclear structure, but the existence of collective rotational transitions does; in particular, it requires rotation around an axis other than the symmetry axis. For a prolate nucleus (or triaxial nucleus favoring prolate shape) rotating around an axis perpendicular to the symmetry axis, the rotational bands are strongly enhanced and favor decay roughly parallel to the yrast line. Thus, they lead to low spins before sufficient cooling takes place to allow observation of the discrete lines (~20 $\hbar$). On the other hand, oblate nuclei (or triaxial nuclei of dominantly oblate shape) rotating around their symmetry axis have their collective transitions suppressed, and so de-excite more steeply into the yrast line. It is reached at a higher spin and, since in this case it is irregular, being composed of single-particle states, not only are discrete states of higher spin observable, but some may be long-lived enough to become isomers, the "yrast traps".

It now appears that both of these types of behavior are observed experimentally. Near the closed-shell neutron numbers 82 and 126 there are a number of near-spherical or slightly oblate nuclei with high-spin states that appear to be made of high-j particles with large projections on the symmetry axis.

Two of the best studied nuclei in the lighter group are ^{152}Dy (refs. 35-38) and ^{154}Er (ref. 39); the level scheme of the former is shown in Fig. 19. Both nuclei show the irregular level spacing and the existence of isomeric states which are characteristic of this noncollective mode of excitation. But

the transition energies are not completely random; with very few exceptions they fall within the limits (700 ± 200) keV. Also, there are no E3 transitions, as might be expected from a pure spherical Nilsson potential, and indeed are seen in the nuclei above ^{208}Pb (^{212}Rn for example). Another aspect, especially apparent in ^{154}Er, is that there are sequences of γ rays of almost constant intensity which are of the same multipolarity and connect levels of the same parity. These two- or three-step sequences have transitions of (600 ± 100) keV with lower energy lines connecting the different sequences. So there are certainly elements of weak collectivity present, waiting for a more detailed understanding.

A striking feature of these level schemes is illustrated in the plot of excitation energy vs $I(I + 1)$ for ^{152}Dy in Fig. 20. Initially the experimental data rise rapidly due to the effect of the pairing correlations, and then at about spin 16 $\hbar$ turn over into an approximately straight line up to the highest spin. The slope of this long straight portion of the curve leads to the determination of an effective amount of inertia through the derivative of Eq. (1).

$$\frac{dE}{d[I(I+1)]} = \frac{\hbar^2}{2\mathcal{J}} \quad . \tag{9}$$

For ^{154}Er this yields $2\mathcal{J}/\hbar^2 = \sim 140$ MeV^{-1} and for ^{152}Dy, ~ 142 MeV^{-1}. These values are 10-15 percent greater than those of a rigid diffuse sphere of the appropriate mass. This increase could be considered an indication of deformation and, if so taken, would correspond to $\beta \approx 0.2$ for a deformed oblate shape,

a rather large deformation. Certainly when collective rotation is considered below, the slope of such a curve, and hence the effective moment of inertia, is thought to bear a connection to the deformation of the nucleus. But here, near a magic number, where the angular momentum is being carried largely by a few particles aligned along the rotation axis, it seems more likely that shell effects will be large and might affect this slope. Results of several recent calclations support this view. For example, Fig. 21 shows curves calculated for several nuclei with neutron numbers around N = 82 using a spherical Nilsson potential and BCS pairing[40], and it can be seen that due to shell effects even larger differences in slopes appear than are seen in experiment. Similar results are found by Leander et al[41], and these authors point out the importance of pairing in calculating these moments of inertia and the configurations of states along the yrast line. Thus, at the present time, it seems likely that slopes such as that in Fig. 20 cannot be used to indicate deformation. Values for these nuclei must be determined by another method.

The measurement of the static quadrupole moment of a state gives clear information about deformation, and such measurements can in principle be made on nanosecond isomers using perturbed angular distribution techniques. The first such determination at high spin for nuclei in this region has been performed on the $(I \sim 49/2^+)$ 500 ns isomer in ^{147}Gd (ref. 42). The quadrupole moment obtained was $(|3.14| \pm 0.17)$b, from which a deformation β of -0.18 was derived (the negative sign was assumed). This is a

reasonably large deformation, two or three times that implied by the aligned particles alone. It is the first real indication that sizeable oblate deformations might exist in this region. Nevertheless, these are very difficult experiments, and more such data are badly needed.

The study of nuclei in this region of the Periodic Table is currently an active research area, and there is hope that a systematics will emerge that can shed more light on the structure of these high-spin states. However, it no longer seems so likely that isomers will be found at spins significantly above these examples (~30 $\hbar$). This is due in part to the steepness of the slope of the yrast line at the higher spin values, but also might be an indication that the strongly oblate shapes are not quite so stable as the present calculations indicate.

Now, for the rest of my talk, I would like to concentrate on continuum spectra, rather than discrete transitions. These will usually involve the opposite situation, namely, rotation of prolate deformed nuclei around an axis at right angles to the symmetry axis, yielding de-excitation by collective rotational bands that run roughly parallel to the yrast line and do not decay into that line until spins of 20-30 $\hbar$ or lower are reached. Thus, all the information we are likely to obtain about the high-spin states must come from continuum studies. Individual transitions cannot be resolved by most present-day techniques (however, see later), but it might be expected that the moments of inertia of these bands would not differ greatly. Then the $I \rightarrow I - 2$ transitions, though not identical, would be

similar in energy and would occur in a limited region of the γ-ray spectrum as given by the rotational expression, Eq. (2), $E_\gamma = (4I - 2)\hbar^2/2\mathcal{J}$. Thus, there is a definite correlation between E_γ and the spin of the de-exciting state, in contrast to the situation with statistical transitions or with the other nonrotational (e.g., vibrational) ones. Figure 22 shows an example of the de-excitation cascades from the 4n product of 181 MeV $^{40}Ar + {}^{126}Te \rightarrow {}^{166}Yb^*$, taken with a 7.6 x 7.6-cm NaI detector in coincidence with a Ge detector gated on the 4n lines.[43] The open squares are the raw pulse-height spectrum, and one can distinguish the high-energy, exponentially falling statistical tail and the lower energy (below 1.5 MeV) yrast bump. The filled points are the same spectrum unfolded, that is, corrected for the NaI response function, to yield the primary γ-ray spectrum, and, in addition, divided by the NaI efficiency and the number of singles in the Ge counter to yield the absolute number of transitions per event per 40 keV interval. The sum of these points is $\bar{M} - 1$, the average multiplicity minus the one trigger γ ray in the Ge detector ($\bar{M} \sim 24$ in this case). The angular anisotropy of the γ rays is shown at the top of the figure. The large anisotropy observed between 800-1400 keV, the region of the yrast bump, indicates almost pure stretched E2 transitions in that bump. The high-energy tail is very similar in a number of nuclei and for a number of bombarding energies and likely corresponds to about half of the 2-4 statistical transitions involved per event. The bump, however, differs from nucleus to nucleus and with bombarding energy. Some evidence

for these two statements is shown at the bottom of Fig. 22. The solid line is the locus of the unfolded points above for 181 MeV ^{40}Ar bombardment. The dotted, short-dashed, and long-dashed lines are similar representations of the continuum spectra from the reactions (331 MeV) $^{86}Kr + ^{80}Sc$, (87 MeV) $^{16}O + ^{150}Sm$, and (157 MeV) $^{40}Ar + ^{126}Te$, respectively, to yield $^{162}Yb + 4n$. These three reactions involve about the same average angular momentum (25-30 $\hbar$) in the γ-ray cascade of the ^{162}Yb product, and the spectra are almost identical. In contrast, the higher energy (181 MeV) ^{40}Ar reaction brings more angular momentum to the cascade (~40 $\hbar$ on average), and the additional γ rays de-exciting these higher spin states move the edge of the bump to a higher transition energy, as expected for rotational bands. If we also know the spins of the highest states, we can determine their effective moments of inertia from Eq. (2). We can, in fact, estimate the spins from the multiplicities, $\bar{I} = 2(\bar{M} - \delta)$ where $\delta = 2$-4 is the number of statistical γ rays assumed to carry out no spin, and the rest of the γ rays are stretched E2 transitions in the case of a good rotor. However, for nonrotational nuclei that have dipoles in their γ cascades, either the factor 2 (the angular momentum carried per γ ray) should be reduced or δ should be increased. There are also other ways to estimate the effective moments of inertia of these continuum high-spin states, some of which will be discussed later, and all methods yield values within 10-20 percent of the rigid-sphere numbers. They are usually larger, suggesting deformation, but this is within the range of errors, both experimental and

theoretical. However, just from the shapes (and changes in shape) of these spectra alone, we have thus obtained an indication of rotational bands, the average multiplicities, and estimates of the moments of inertia at high spin.

But can we observe the suggested rotational correlation between γ-ray energy and spin more directly? A powerful technique is the measurement of average γ-ray multiplicities as a function of transition energy. Gamma-ray multiplicities can be measured in a number of ways, some of which have become increasingly sophisticated in recent years. But the early technique is quite straightforward, requiring only a trigger counter in coincidence with the detector in which the spectrum is being measured. Then

$$\frac{N_c}{N_s} = 1 - \left[1 - \frac{\omega}{1-\Omega}\right]^{\langle M-1\rangle} \xrightarrow[\Omega \gtrsim 0]{\omega \gtrsim 0} \langle M - 1\rangle\omega \qquad (10)$$

where N_c and N_s are the coincidence and singles counting rates in the trigger counter, ω and Ω are the efficiencies (including solid angle, γ-efficiency, angular correlation, conversion coefficient, etc.) of the detector and trigger counters, respectively, and $\langle M\rangle$ is the desired average γ-ray multiplicity.[44-49]

If instead of the single trigger counter, a number of counters are used, and the number of these counters that are coincident in each event is recorded, one has a "multiplicity filter". These have been given a variety of names depending upon their geometrical appearance: porcupine, halo, hedgehog, urchin, etc.[45,50-52] From the ratios of the intensities of the

various folds (events with the same number of trigger counters), not only the average multiplicity can be determined, but also the second moment, $\langle M^2 \rangle - \langle M \rangle^2$, the square of the width of the distribution in M, and, in principle, still higher moments. A number of algorithms have been developed to obtain these moments from the experimental fold distributions.[50,52-56] A high γ-ray multiplicity corresponds in general to a large angular momentum, although the exact relationship may not always be clear. But because of this relationship, a measurement of average γ-ray multiplicity as a function of γ-ray transition energy gives direct information on transition energy-spin correlations in the continuum.[57,58]

Such spectra for the system $^{40}Ar + ^{124}Sn \rightarrow ^{164}Er^*$ at several bombarding energies are shown[58] in Fig. 23. There is a pronounced peak at all bombarding energies, and it comes at the upper edge of the yrast-like transitions in the γ-ray spectrum shown above. This multiplicity peak shows clearly that the highest energy yrast-like transitions are associated with the highest spins populated. The right side of Fig. 23 shows γ-ray spectra and multiplicity spectra calculated using a very simple model; a purely rotational yrast-like cascade is assumed. All the significant observed features are reproduced. This provides a rather direct confirmation of the collective rotor picture for this nucleus, all the way from the discrete transitions near the ground state to the highest spins observed, about 60 ħ. The moment of inertia used in the calculation was roughly the rigid-body value and was constant over the whole spin range.

This suggests that the deformation of ^{160}Er remains prolate, $\beta \sim 0.3$, up to the highest spins.

Away from the deformed rotors, there is a more complex behavior. The $^{40}Ar + ^{82}Se \rightarrow ^{122}Te^*$ system (Fig. 24a) does not show a peak in the multiplicity spectrum at 121 or 131 MeV, but develops one at still higher bombarding energies. The major reaction product at these energies, ^{118}Te, has a ground band with roughly equidistant level spacing up to spin 14 $\hbar$ (quasi-vibrational). There are stretched E2 transitions between these levels which are weakly collective but certainly not rotational. Above 150 MeV bombarding energy (spin 30-35 $\hbar$), a peak appears in the multiplicity spectrum and moves to higher transition energy with increasing ^{40}Ar energy. This is an indication of the onset of rotational behavior. A calculation can reproduce this feature if a rotational spectrum is assumed for $I > 35\ \hbar$, and an uncorrelated spectrum below this spin. The $^{48}Ca + ^{100}Mo \rightarrow ^{148}Sm^*$ system shown in Fig. 24b is a striking example; the nearly semi-magic product nuclei do not show formation of a rotational peak until about spin 50 $\hbar$.

All of these nuclei appear to become rotational at some spin. The behavior of ^{152}Dy and ^{154}Er is interesting in this respect since they are outstanding examples of nonrotational decay from weakly oblate nuclei up to nearly 40 $\hbar$. A group at Orsay[59] has studied ^{154}Er in comparison with ^{160}Er by bombarding targets of ^{119}Sn and ^{124}Sn with ^{40}Ar beams of appropriate energy. The ^{164}Er compound nucleus has a γ-ray spectrum (Fig. 25) showing the characteristic yrast bump below 1.6 MeV with a flat region below 1 MeV. The ^{159}Er compound

nucleus has a very different spectrum showing two bumps below 1.6 MeV separated by a valley at about 1 MeV. The low-energy bump has a high intensity and contains all the known discrete transitions around 0.7 MeV connecting states with spins up to 36 $\hbar$. The higher bump starts at ~1 MeV, and above its maximum at 1.3 MeV seems to resemble the upper part of the rotational bump in the ^{159,160}Er product nuclei. This second bump develops very strongly with increasing fold number, showing that it comes from high-spin states. The multiplicity spectrum for the ^{154,155}Er products also shows two peaks. The multiplicity estimated for the upper peak, 31, indicates again that it comes from the highest spin states in the cascade, and there is a remarkable similarity to the upper part of the ^{159,160}Er multiplicity spectrum. The multipole composition of the γ-ray spectra, deduced from the 0° and 90° intensities with the assumption of only stretched dipole and quadrupole transitions, shows the upper bump in ^{154,155}Er consists mainly of stretched quadrupole transitions. This is not true for the lower peak, which has a large fraction of dipoles, in agreement with the known discrete lines in ^{154,155}Er. The calculated spin at the top of the cascade is ~60 $\hbar$ and the effective moment of inertia is ~150 MeV^{-1}. The evidence seems quite good that, at about spin 40 $\hbar$, the products ^{154,155}Er switch from weakly oblate nuclei to rather strongly deformed (most likely rotational) nuclei. The experimental results do not determine whether these shapes are oblate or prolate, but the similarities with the heavier Er nuclei suggest the latter.

Although the number of cases studied is still quite small, the experimental evidence indicates that nuclei in the mass region 100-170 deform (if not deformed already in the ground state) and show rotational behavior above some spin which depends on the detailed structure of the particular nucleus. There appears to be a rather systematic behavior. The N = 82 and nearby nuclei have mostly dipole transitions at low energies and only begin to rotate at very high spins (40-60 $\hbar$). The quasi-vibrational nuclei have more stretched E2 radiation at low energies, which is weakly collective but not rotational. They deform and become rotational at lower spins (35-45 $\hbar$). Finally, there are well-deformed prolate nuclei which show a high proportion of collective stretched E2 transitions at all spins.

Continuum γ-ray measurements are not as precise and as unambiguous as discrete line studies. So a variety of techniques must be used to obtain as many different insights as possible. A number of different types of studies have been carried out: conversion electron measurements[60], plane polarization studies[61-63], angular correlation studies[64], and Doppler-shift lifetime measurements[65]. All yield some interesting results; however, I will not have time to discuss them but will pass on to moment-of-inertia determinations.

As already mentioned, determination of the energy of the edge of the yrast bump and the corresponding maximum spin gives a value for $\mathcal{J}_{eff}$ at the top of the cascade. To obtain additional values at lower spins, the bombarding energy can be lowered. Or, in the lower spin region of a spectrum where the

population is constant (i.e., every cascade goes through that region—for example, in a 3n channel at angular momenta where the corresponding ℓ waves lead mainly to the 4n and 5n channels), a spin value can be obtained for any transition energy by summing the number of transitions up to that point and using $I = 2(M - \delta)$ where δ now refers only to the statistical transitions under the region summed. Some estimates for the effective moment of inertia obtained by these methods are shown[43] in Fig. 26 for the product nucleus ^{162}Yb. The small dots give the values for the known discrete ground-band transitions, and the open circles are for the isotone ^{160}Er which is known through the backbend. The four points with error bars are calculated by the "edge method" at different bombarding energies, and the large dots connected by a solid line are from the method just described.

Both of these methods depend upon associating a given γ-ray energy with a particular spin value. There also exists a "differential" method which utilizes an expression derived from Eq. (2) for stretched E2 transitions:

$$\Delta E_\gamma = 8\hbar^2/2\mathcal{J} - 2E_\gamma d\ln\mathcal{J}/dI \quad . \tag{11}$$

For a reasonably constant moment of inertia, this becomes:

$$\Delta E_\gamma = 8\hbar^2/2\mathcal{J} \, . \tag{12}$$

The energy difference, ΔE_γ, can be obtained simply from the height of the γ-ray spectrum. For example, on the unfolded spectrum of Fig. 22, the height of the spectrum gives the number of rotational transitions (n_γ) per energy interval (0.040 MeV in Fig. 22) per event. The reciprocal, $0.040/n_\gamma$, is the

average difference between adjacent transition energies, ΔE_γ, and can be related to the moment of inertia by Eq. (12). The values so calculated are also shown in Fig. 26 as diamonds connected by a dashed line. This method also requires a constant population in the region of application, and so has a limited range of use (between 0.7 and 1.0 MeV in Fig. 22). The values from the different methods (Fig. 26) are in reasonably good agreement, and above spin 20 $\hbar$ [$(\hbar\omega)^2 \approx 0.12$ MeV] are within ten percent of the value for a rigid diffuse sphere of mass 162. The uncertainties in these values are at least that large, so the results agree with this simple estimate as well as can be expected using this approach.

A newer study[66] using these methods determines the edge energy from the multiplicity peak in plots of M_γ vs E_γ, as in Figs. 23,24; these peaks are sharper than the yrast bump edge in γ-ray spectra and so permit a more definitive evaluation. However, the problem is always to obtain the property of interest (in this case $\bar{E}_\gamma$ and $\bar{I}$) for the smallest range in spin possible. With the presently available techniques this range is never small. One of the best ways is to use a total-energy spectrometer[67], although this still means a FWHM of 60-70% in spin. The idea is as follows: if one can capture in a large NaI counter most of the γ-ray energy emitted in the cascades, one can then make cuts or slices at various excitation energies, hence at various spin ranges, and observe the decay spectrum in a coincident external counter viewing the target through a small hole in the sum spectrometer. The type of slicing is shown in

Fig. 27; the higher excitation energy slices also correspond to higher spin regions, but unfortunately even a narrow slice corresponds to a wide range of spin because of the shape of the region populated. Examples[68] of the spectra taken in a 7.5 x 7.5 cm NaI crystal outside a sum spectrometer and in coincidence with consecutive ~4 MeV wide slices of the total excitation energy are shown[68] at the top of Fig. 28 for 185 MeV ^{40}Ar + $^{124}Sn \rightarrow {}^{164}Er^*$. The main reaction products, ^{160}Er and ^{159}Er, are deformed prolate nuclei in the ground and $i_{13/2}$ bands, respectively, all the way to the highest spins observed. In the first few spectra, the increase in average angular momentum associated with higher sum energy causes an increased yield of essentially all γ rays. After about slice 5 the yield of the lower energy transitions ($E_\gamma < 0.6$ MeV, $I < 20$) is saturated because the feeding occurs at higher energy (higher spin). The movement of the yrast-bump edge to higher energy then becomes noticeable, and by subtracting the spectrum of one slice from the next one, the curves in the bottom of the figure are obtained. Their centroids can be considered to be the average edge, $\overline{E}_\gamma$, for the spectra of the two consecutive slices. The corresponding spin, $\overline{I}$, can be obtained from the average multiplicity for the two spectra determined in the same measurement. However, the multiplicity measurement does have a complication. For a perfect sum spectrometer with 100% efficiency and 4π geometry if the external counter is included, the ratio of coincidence counts with the external counter to singles counts in the sum detector can be written

$$N_c/N_s = 1 - (1 - \omega)^M \quad , \tag{13}$$

much like Eq. (10), where ω is the solid angle of the external E_γ detector. In a real sum spectrometer there will be losses due to detector transparency and geometry, $\Omega < 4\pi$, and the multiplicity will depend upon the actual energy collected. This can be accounted for if the ratio of coincidence to single events is calculated both with the external detector spectrum added to the sum spectrometer one, $(N_c/N_s)_{\Omega+\omega}$ and with just the sum spectrometer spectrum $(N_c/N_s)_\Omega$

$$(N_c/N_s)_{\Omega+\omega} = 1 - (1 - \frac{\omega}{\omega+\Omega})^X \tag{14}$$

$$(N_c/N_s)_\Omega = 1 - (1 - \frac{\omega}{1-\Omega})^{M-X} \tag{15}$$

where X is the number of γ rays out of M that actually are collected in the sum spectrometer. The average multiplicity M can then be obtained by eliminating X between the two expressions. For large enough Ω ($\Omega > 0.5$), this yields

$$\overline{M} \approx (N_c/N_s)_{\Omega+\omega} \cdot \frac{(\omega + \Omega)}{\omega} + (N_c/N_s)_\Omega \frac{(1 - \Omega)}{\omega} \quad . \tag{16}$$

If the sum crystal is divided into sectors and a requirement is made that several or all of these must fire for an event to be recorded, the expressions become more complicated and require a numerical solution (e.g. ref. 69). But in any case, a determination of $\overline{M}$ yields a value for $\overline{I}$, which when substituted with the corresponding value of $\overline{E}_\gamma$ into Eq. (2) gives an effective moment of inertia for that γ-ray energy. Values so determined for the compound system $^{164}Er^*$ are shown in Fig. 29. An important advantage of this method is that the "average" edge

and the multiplicity are both determined objectively and correspond to the same input distribution of angular momentum. Also no extrapolation from average to maximum angular momentum is required.

A type of differential method can also be applied to the spectra obtained in coincidence with slices of the total-energy spectrum. The area of each difference peak (bottom of Fig. 28) gives the incremental number of rotational transitions (half the angular momentum increase ΔI) and the difference in the centroids of two consecutive peaks gives the average increase in transition energy, $\Delta\bar{E}_\gamma$. Use of Eq. (11) then gives effective moments of inertia which depend essentially on the difference in multiplicities rather than on the multiplicities themselves, and so provides a partially independent evaluation of $\mathcal{J}$. As can be seen in Fig. 29, the integral and differential methods are in good agreement.

This sum-crystal method probably provides the most reliable values presently available for moments of inertia at very high spin. They are in rather close agreement with the liquid-drop model—about 10 percent or so above the rigid-sphere values. A few measurements have been made for comparable spin ranges outside the rare-earth region. They also seem to be near the liquid-drop value. Very careful studies are under way at present to look for the large increase in moment of inertia at the very highest spins that has been predicted by the liquid-drop model and might be reinforced in some regions by shell effects.

But the moment of inertia described so far is an "effective" one; it is measured along the average of the γ-cascade pathways, and so is an average envelope for many intersecting (crossing) bands, as shown in Fig. 30. The collective moment of inertia of an individual band is smaller and corresponds to its greater curvature in the plot. It is related to differences between γ-ray energies in the same band, and not to the difference between average γ-ray energies in a pathway (several intersecting bands). The angular momentum in these excited bands is carried partly by the rotation of the deformed nucleus as a whole and partly by a few high-j nucleons aligned to the rotation axis. The energy in one such rotational band is given by

$$E(I) = \frac{\hbar^2}{2\mathcal{J}_{coll}} R^2 + E(j_a) = \frac{\hbar^2}{2\mathcal{J}_{coll}} (I - j_a)^2 + E(j_a) \ , \quad (17)$$

where $\mathcal{J}_{coll}$ is the moment of inertia of the collective rotation of the nucleus, j_a is the aligned angular momentum of the nucleons, $E(j_a)$ is the bandhead energy, and 1 is neglected compared to $I - j_a$. The assumptions made in Fig. 30 are that $\mathcal{J}_{coll}$ and j_a are approximately constant in a band and only $E(j_a)$ and j_a change between bands. The γ-ray transition energy within the band is then

$$E_\gamma = \frac{\hbar^2}{2\mathcal{J}_{coll}} 4(I - j_a) \ , \quad (18)$$

to be compared with the corresponding form of Eq. (2)

$$E_\gamma = \frac{\hbar^2}{2\mathcal{J}_{eff}} 4I \ , \quad (19)$$

which gives the envelope of the bands without reference to any alignment. The relationship between the two moments of inertia is then

$$\mathcal{J}_{eff} = \frac{I}{I-j_a}\mathcal{J}_{coll} \quad . \tag{20}$$

Since j_a is expected to be large—around one-half of I in the backbend region and probably not relatively smaller at higher spins—$\mathcal{J}_{coll}$ must be much smaller than $\mathcal{J}_{eff}$, reflecting the fact that a single particle cannot contribute fully both to the aligned angular momentum and to the collective moment of inertia. Only I and E_γ are usually measured, so it is $\mathcal{J}_{eff}$ that is normally determined and found to be roughly equal to the rigid-body value.

Can $\mathcal{J}_{coll}$ be determined experimentally? There is some evidence and some hope that this can be done by studies of γ-γ energy correlations. Consider a nucleus de-exciting through a rotational cascade with a fixed moment of inertia, a true rigid rotor. Then by Eq. (2) the γ-ray spectrum is a set of transitions, evenly spaced at $8\hbar^2/2\mathcal{J}$, as shown in Fig. 31a. If this cascade is looked at by two γ counters, and the first one is gated on a particular transition, the coincident spectrum in the second counter looks as shown in Fig. 31b. One sees the whole spectrum, but for the gated line. If, instead of a single value for $\mathcal{J}$, there are many cascades with a small spread in $\mathcal{J}$, then the lines become a distribution of transitions that widen as they leave the vicinity of the gate energy, Fig. 31c. But the distance between the peaks on each side of the missing gate is

still equal to 16 $\hbar^2/2\mathcal{J}_{coll}$ and the spread in the peaks gives the initial spread in values of $\mathcal{J}$.

A schematic two-dimensional spectrum of one coincident γ-ray detector against another for a rotational nucleus is shown in Fig. 32. The dots represent the location of coincidences betwen γ-rays' de-exciting states up to I = 14 in a perfect rotational band with moment of inertia $\mathcal{J}$. However, different bands might have somewhat different moments of inertia, and the lines through the dots represent bands having moments of inertia differing by ±10 percent from $\mathcal{J}$. It is also well known that nuclei align angular momentum at relatively low spin values, and the crosses in Fig. 32 are coincidences between transitions from spins 16 to 26 $\hbar$ in a band having 11 $\hbar$ aligned, also with a moment of inertia $\mathcal{J}$. The light lines through the crosses again represent aligned bands differing in $\mathcal{J}$ by ±10 percent. It is clear that even if bands are populated that differ considerably in moment of inertia and aligned angular momentum, a stong pattern remains in the two-dimensional γ-γ coincidence spectrum. The valley along the diagonal, representing the absence of transitions of the same energy, is not at all filled, and the first ridge adjacent to it is rather clear. (Notice, however, that a single band with a <u>changing</u> moment of inertia or alignment has not been considered.) It is then of considerable interest to know whether these correlations are present in real spectra at very high spins.

To perform such correlation experiments requires good statistics and a method to reduce the number of uncorrelated

events. The first successful experiment was made by Andersen et al[70]. They used four detectors, resulting in six independent pairs and, after equalizing the gains, plotted every coincidence on a single two-dimensional array. A background of uncorrelated events was subtracted from the γ-γ matrix. Basically this background is calculated for the point ij from the projections of the row, $\sum_k N_{ik}$, and the column, $\sum_l N_{lj}$, on the assumption that every uncorrelated γ ray is equally probably in coincidence with every other observed one. The correlated two-dimensional spectrum is then

$$\Delta N_{ij}(E_i,E_j) = N_{ij} - \frac{\sum_k N_{ik} \sum_l N_{lj}}{\sum_{lk} N_{lk}} \quad . \tag{21}$$

However, the background subtracted in Eq. (21) is too large, since the projections $\sum_k N_{ik}$ and $\sum_l N_{lj}$ also contain the correlated events. An iteration procedure may be used; the projections of the absolute values of the correlated array $\sum_k |\Delta N_{ik}|$ and $\sum_l |\Delta N_{li}|$ give a first approximation to the number of correlated events in a row and column and can be used to correct the background subtraction

$$\Delta N_{ij}(E_i,E_j)_{p+1} = N_{ij} - \frac{\sum_k (N_{ik} - |\Delta N_{ik}|_p) \sum_l (N_{lj} - |\Delta N_{lj}|_p)}{\sum_{lk} (N_{lk} - |\Delta N_{lk}|_p)} \tag{22}$$

where Eq. (21) is the first step with p = 0. There are still some problems with this subtraction method, and others are being explored, but it appears that the basic results found are not much affected by

these problems. An additional correction is to divide each point by the corresponding relative detector efficiency. The original experiments were limited by beam energies to rather low angular momenta. I will show a later study[71] applying this method to a system where the maximum angular momentum the nucleus can hold was brought in.

The correlated spectrum (without iterated background subtraction or efficiency correction) for the system $^{124}Sn + {}^{40}Ar \rightarrow {}^{164}Er^*$ at 185-MeV ^{40}Ar energy is shown in Fig. 33. Four features, believed to be general, can be pointed out. First, there is a distinct valley along the diagonal up to about 1 MeV (spin 40 $\hbar$) having a measurable width, and there is some possibility this valley also exists in the region above 1.1 MeV. Second, there are a few bridges across this valley beginning as low as 0.55-0.60 MeV, and continuing as far up as the valley persists. Also there are irregularities in the ridges along the this valley. Third, there is a general filling of the valley above ~1 MeV, which is rather complete around 1.1 MeV. Finally, there are stripes or lines of increased intensity running parallel to the coordinate axes. This last feature is better seen in Fig. 34 (for $^{0}Ar + {}^{130}Te \rightarrow {}^{170}Yb^*$) which has had the background subtraction iterated 16 times and has been efficiency corrected. There are other features in Figs. 33 and 34 that one would hope to understand; however, thus far only these four have been considered.

The mere existence of the valley strongly indicates the rotational nature of the bands for this range of γ-ray transition energies. In addition, the half-width of the valley is just the difference between successive transition energies. Assuming again that these occur within a band of constant $\mathcal{J}_{coll}$ and j_a,

$$\Delta E_\gamma = 8 \frac{\hbar^2}{2\mathcal{J}_{coll}} \quad , \tag{23}$$

and the valley width equals $16\,\hbar^2/2\mathcal{J}_{coll}$ and so determines $\mathcal{J}_{coll}$. The first results[71] on this point suggest that $\mathcal{J}_{coll}$ is indeed smaller than $\mathcal{J}_{eff}$, with values as low as ~0.6 $_{eff}$. These results are tentative, but if $\mathcal{J}_{coll}$, $\mathcal{J}_{eff}$, and I can be reliably measured, then j_a can be determined via Eq. (23). This would be a very interesting quantity to know for the high-spin states.

The lowest energy bridges in Fig. 33 are due to known backbends in the nuclei produced. The large one at 0.55 MeV (ω ~ 0.27 MeV) corresponds to the first backbends in ^{158}Er and ^{160}Er (the major even-even products). Backbending or upbending behavior implies several γ rays of similar energies in the band and thus tends to fill the valley. The arguments developed in connection with Fig. 14 have demonstrated that a given level crossing will show up in many bands at the same rotational frequency (the same γ-ray energy). This must be true for the second large bridge at ~0.8 MeV (ω ~ 0.42 MeV), at the location of the second backbend in ^{158}Er, since the population of that backbend in the yrast sequence is quite weak but the bridge is a prominent feature. It is known that the first backbend in this region of nuclei involves the alignment of two $i_{13/2}$ neutrons, and the second probably the alignment of two $h_{11/2}$ protons. There are at least two more higher energy bridges in Fig. 33, each of which must involve many bands since they have not been observed in any discrete-line studies. It is not yet clear which orbitals are

involved in these higher bridges. However, the general behavior up to about 1-MeV γ-ray energy seems reasonably clear—a deep valley reflecting good rotational behavior, and a few large irregularities in both the valley and ridge structure resulting from alignment of specific high-j orbitals. Similar behavior is observed in Fig. 34 for the ^{170}Yb compound system.

Above 1 MeV in Figs. 33 and 34, the valley is largely filled and completely so in places. It is not really clear what causes this, but a reasonable extension of the features described above seems able to account for it. The levels calculated for protons by rotating a prolate potential was shown in Fig. 13. The erbium nuclei produced here have 68 protons, the ytterbinum nuclei have 70, so the Fermi level is in a basically N = 4 shell into which an N = 5 ($h_{11/2}$) orbital has intruded. If the 68-70 proton region (around the level 523,7/2) in Fig. 13 is followed to higher frequency, it intersects some strongly downsloping levels at $\omega/\omega_0 \approx 0.07$ ($E_\gamma \approx 1.1$ MeV for A = 160). These levels come from the shell above (N = 5 with N = 6 intruder), and in fact correspond to the highest aligned $i_{13/2}$ (N = 6) components together with the most aligned $h_{9/2}$ level. An N = 6 level coming down into the basically N = 4 shell ($\Delta N = 2$) is particularly interesting since it has the same parity and thus can mix into these levels. The neutrons in this region do the same thing (N = 7 ($j_{15/2}$) coming into the N = 5 shell) at about the same frequency. Thus one might expect level crossings and very distrubed rotational bands. Perhaps this can account for the general filling of the valley in this region. If true, it

could be a reasonably general phenomenon implying tendencies for the nucleus to become more triaxial and more deformed. It will be interesting to try to verify such behavior.

Finally, we come to the stripes parallel to the coordinate axes, as illustrated in Fig. 34. Those at lower γ-ray energies involve the known backbends; because of the increased number of transitions of the same energy, there is a marked increase in the intensity of the row and column passing through the backbend peak along the diagonal. It seems likely that the same effect explains the higher energy stripes, except that the intensity at the backbend or upbend may come not from a single band crossing, but from a number of (excited) bands that cross at approximately the same rotational frequency (as discussed earlier). For a cascade with multiple backbends (upbends), the coincidences between them occur at the intersection of a horizontal and vertical stripe, and will stand out in the iterated spectrum as a peak due to the increased intensity of both backbend (upbend) regions. It should be noted that the peaks and stripes we are discussing constitute only a few percent of the intensity of the original data array before background subtractions are made and iterated. There may be other explanations for such small peaks and stripes.

But these E_γ-E_γ correlation experiments represent a frontier in the continuum work. There are detailed features in the spectra of Figs. 33 and 34 that are not yet understood, and the cause for the filling of the valley at high spins and the origin of the stripes above 1 MeV represent major effects to be

studied. This kind of experiment has also been done in coincidence with an energy-sum spectrometer, in order to concentrate the observed population more on the highest spins, and there is the possibility of doing triple correlations and of employing 4π crystal-ball detectors. Such correlation studies seem to offer real hope for a detailed understanding of high-spin states.

Acknowledgements

I would like to thank all the visitors to our group and the collaborators during the last few years who have contributed so much to the experiments described in these lectures and to so many helpful and informative discussions. But that list would be too lengthy so I shall list only those involved during the past year: O. Andersen, M. A. Deleplanque, E. Dines, J. Draper, C. Ellegaard, J. Garrett, B. Herskind, H. Kluge, J. O. Newton, C. Schuck, S. Shih, and especially my partner, F. S. Stephens.

References

1. A. Bohr, Phys. Rev. 81, 134 (1951); Mat. Fys. Medd. Dan. Vid. Selsk. 26: No. 14 (1952).
2. D. Ward, P. Colombani, I.Y. Lee, P.A. Butler, R.S. Simon, R.M. Diamond, and F.S. Stephens, Nucl. Phys. A266, 194 (1976).
3. P. Fuchs, H. Emling, F. Folkmann, E. Grosse, D. Schwalm, R.S. Simon, H.J. Wollersheim, J. Idzko, and D. Pelte, Jahresbericht 1977, G.S.I. p. 65.
4. M. Guidry, P.A. Butler, P. Colombani, I.Y. Lee, D. Ward, R.M. Diamond, F.S. Stephens, E. Eichler, N.R. Johnson, and R. Sturm, Nucl. Phys. A266, 228 (1976).
5. A. Bohr, B. Mottelson, and D. Pines, Phys. Rev. 110, 936 (1958).
6. J.J. Griffin and M. Rich, Phys.Rev. 118, 850 (1960).
7. S.G. Nilsson and O. Prior, Mat. Fys. Medd. Dan. Vid. Selsk. 32: No. 16 (1961).
8. M.A.J. Mariscotti, G. Scharff-Goldhaber, and B. Buck, Phys. Rev. 178, 1864 (1969).
9. S.H. Harris, Phys. Rev. 138, B509 (1965).
10. A. Johnson, H. Ryde, and J. Sztarkier, Phys. Lett. 34B, 605 (1971).
11. Nucl. Data Tables, Sec. A, 11, 327 (1974).
12. F.S. Stephens and R.S. Simon, Nucl. Phys. A183, 257 (1972).

13. I.Y. Lee, D. Cline, R.S. Simon, P.A. Butler, P. Colombani, M.W. Guidry, F.S. Stephens, R.M. Diamond, N.R. Johnson, and E. Eichler, Phys. Rev. Lett. 37, 426 (1976); S.W. Yates, I.Y. Lee, N.R. Johnson, E. Eichler, L.L. Riedinger, M.W. Guidry, A.C. Kahler, D. Cline, R.S. Simon, P.A. Butler, P. Colombani, F.S. Stephens, R.M. Diamond, R.M. Ronningen, R.D. Hichwa, J.H. Hamilton, and E.L. Robinson, Phys. Rev. C21, 2366 (1980).

14. O.C. Kistner, A.W. Sunyar, and E. der Mateosian, Phys. Rev. C17, 1417 (1978).

15. C. Flaum and D. Cline, Phys. Rev. C14, 1224 (1976).

16. E. Grosse, F.S. Stephens, and R.M. Diamond, Phys. Rev. Lett. 31, 840 (1973).

17. E. Grosse, F.S. Stephens, and R.M. Diamond, Phys. Rev. Lett. 32, 74 (1974).

18. I.Y. Lee, M.M. Aleonard, M.A. Deleplanque, Y. El Marri, J.O. Newton, R.S. Simon, R.M. Diamond, and F.S. Stephens, Phys. Rev. Lett. 38, 1454 (1977).

19. L.L. Riedinger, O. Andersen, S. Frauendorf, J.D. Garrett, J.J. Gaardhøje, G.B. Hagemann, M. Guttormsen, B. Herskind, Y.V. Makovetzky, P.O. Tjøm, and J.C. Waddington, Phys. Rev. Lett. 44, 568 (1980.

20. S.G. Nilsson, Dan. Mat. Fys. Medd. 29, No. 16 (1955).

21. V.M. Strutinsky, Yad. Fiz. 3, 614 (1966); transl. Sov. J. Nucl. Phys. 3, 449 (1966).

22. R. Bengtsson, S.E. Larson, G. Leander, P. Moller, S.G. Nilsson, S. Åberg, and Z. Szymanski, Phys. Lett. 57B, 301 (1975).

23. K. Neergaard and V.V. Pashkevich, Phys. Lett. 59B, 218 (1975).

24. C.G. Andersson, S.E. Larson, G. Leander, P. Moller, S.G. Nilsson, I. Ragnarsson, S. Åberg, R. Bengtsson, J. Dudek, B. Nerlo-Pomarska, K. Pomorski, and Z. Szymanski, Nucl. Phys. A268, 205 (1976).

25. K. Neergaard, V.V. Pashkevich, and S. Frauendorf, Nucl. Phys. A262, 61 (1976).

26. K. Neergaard, H. Toki, M. Ploszajczak, and A. Faessler, Nucl. Phys. A287, 48 (1977).

27. H.J. Mang, Phys. Rep. 18, 325 (1975).

28. A. Faessler, K.R.S. Devi, F. Grummer, K.W. Schmid, and R.R. Hilton, Nucl. Phys. A256, 106 (1976).

29. A.L. Goodman, Adv. Nucl. Phys. 11, 263 (1979).

30. R. Bengtsson and S. Frauendorf, Nucl. Phys. A314, 27 (1979); A327, 139 (1979).

31. S. Cohen, F. Plasil, and W.J. Swiatecki, Ann. Phys. 82, 557 (1974).

32. W.D. Myers, Nucl. Phys. A204, 465 (1973).

33. J. Blocki, J. Randrup, W.J. Swiatecki, and C.F. Tsang, Ann. Phys. 105, 427 (1976).

34. A. Bohr and B.R. Mottelson, Nuclear Structure Vol. 2, W.A. Benjamin, Inc., Reading, Mass. 1975.

35. T.L.Khoo, R.K. Smither, B. Haas, O. Häusser, H.R. Andrews, D. Horn, and D. Ward, Phys. Rev. Lett. 41, 1027 (1978).

36. J.C. Merdinger, F.A. Beck, T. Byrski, C. Gehringer, J.P. Vivien, E. Bozek, and J. Styczen, Phys. Rev. Lett. 42, 23 (1979).

37. B. Haas, H.R. Andrews, O. Häusser, P. Horn, J.F. Sharpey-Schafer, P. Taras, W. Trautmann, D. Ward, T.L. Khoo, and R.K. Smither, Phys. Lett. 84B, 178 (1979).

38. P. Aguer, G. Bastin, A. Charmant, Y. El Masri, P. Hubert, R. Janssens, C. Michel, J.P. Thibaud, and J. Vervier, Phys. Lett. 82B, 55 (1979).

39. C. Baktash, E. der Mateosian, O.C. Kistner, and A.W. Sunyar, Phys. Rev. Lett. 42, 637 (1979).

40. L. Moretto, unpublished work, 1979.

41. G. Leander, C.G. Andersson, S.G. Nilsson, I. Ragnarsson, S. Åberg, J. Almberger, T. Døssing, and K. Neergaard, Proc. Symposium on High-Spin Phenomena in Nuclei, ANL/PHY-79-4, p. 197, Argonne, Ill.

42. O. Häusser, H.-E. Mahnke, J.F. Sharpey-Schafer, M.L. Swanson, P. Taras, D. Ward, H.R. Andrews, and T.K. Alexander, Phys. Rev. Lett. 44, 132 (1980).

43. R.S. Simon, M.V. Banaschik, R.M. Diamond, J.O. Newton, and F.S. Stephens, Nucl. Phys. A290, 253 (1977).

44. P.O. Tjøm, F.S. Stephens, R.M. Diamond, J. deBoer, and W.E. Meyerhof, Phys. Rev. Lett. 33, 396 (1974).

45. G.B. Hagemann, B. Broda, B. Herskind, M. Ishihara, S. Ogaza, and H. Ryde, Nucl. Phys. A245, 166 (1975).

46. E. der Mateosian, O.C. Kistner, and A.W. Sunyar, Phys. Rev. Lett. 33, 596 (1974).

47. J.O. Newton, J.C. Lisle, G.D. Dracoulis, J.R. Leigh, and D.C. Weisser, Phys. Rev. Lett. 34, 99 (1975).

48. W. Trautmann, D. Proetel, O. Häusser, W. Hering, and F. Riess, Phys. Rev. Lett. 35, 1694 (1975).

49. M. Fenzl and O.W.B. Schult, Z. Phys. 272, 207 (1975).

50. O. Andersen, R. Bauer, G.B. Hagemann, M.L. Halbert, B. Herskind, M. Neiman, H. Oeschler, and H. Ryde, Nucl. Phys. A195, 163 (1978).

51. D.G. Sarantites, J.H. Barker, M.L. Halbert, D.C. Hensley, R.A. Dayras, E. Eichler, N.R. Johnson, and S.A. Gronemeyer, Phys. Rev. C14, 2138 (1976).

52. L. Westerberg, D.G. Sarantites, R. Lovett, J.T. Hood, J.H. Barker, C.M. Currie, and N. Mullani, Nucl. Instr. 145, 295 (1977).

53. S.Y. Van der Werf, Nucl. Instr. 153, 221 (1978).

54. W.J. Ockels, Z. Phys. A286, 181 (1978).

55. W. Kohl, D. Kolb, and I. Giese, Z. Phys. A285, 17 (1978).

56. A. Kerek, J. Kihlgren, Th. Lindblad, C. Pomar, J. Sztarkier, W. Walus, Ö. Skeppstedt, J. Bialkowski, J. Kownacki, Z. Sujkowski, and A. Zglinski, Nucl. Inst. 150, 483 (1978).

57. J.O. Newton, I.Y. Lee, R.S. Simon, M.M. Aleonard, Y. El Masri, F.S. Stephens, and R.M. Diamond, Phys. Rev. Lett. 38, 810 (1977).

58. M.A. Deleplanque, I.Y. Lee, F.S. Stephens, R.M. Diamond, and M.M. Aleonard, Phys. Rev. Lett. 40, 629 (1978).

59. M.A. Deleplanque, J.P. Husson, N. Perrin, F.S. Stephens, G. Bastin, C. Schuck, J.P. Thibaud, L. Hildingsson, S. Hjorth, A. Johnson, and Th. Lindblad, Phys. Rev. Lett. 43, 1001 (1979).

60. S.J. Feenstra, W.J. Ockels, J. van Klinken, M.J.A. deVoigt, and Z. Sujkowski, Phys. Lett. 69B, 403 (1977); S.J. Feenstra, J. van Klinken, J.P. Pijn, R. Janssens, C. Michel, J. Steyaert, J. Vervier, K. Cornelis, M. Huyse, and G. Lhersonneau, Phys. Lett. 80B, 183 (1979).

61. J.P. Vivien, Y. Schutz, F.A. Beck, E. Bozek, T. Byrski, C. Gehringer, and J.C. Merdinger, Phys. Lett. 85B, 325 (1979).

62. W. Trautmann, J.F. Sharpey-Schafer, H.R. Andrews, B. Haas, O. Häusser, P. Taras, and D. Ward, Phys. Rev. Lett. 43, 991 (1979).

63. H. Hübel, R.M. Diamond, F.S. Stephens, B. Herskind, and R. Bauer, Z. Phys. to be published, 1980.

64. M.A. Deleplanque, T. Byrski, R.M. Diamond, H. Hübel, F.S. Stephens, B. Herskind, and R. Bauer, Phys. Rev. Lett. 41, 1105 (1978).

65. H. Hübel, U. Smilansky, R.M. Diamond, F.S. Stephens, and B. Herskind, Phys. Rev. Lett. 41, 791 (1978).

66. D.L. Hillis, J.D. Garrett, O. Christensen, B. Fernandez, G.B. Hagemann, B. Herskind, B.B. Back, and F. Folkmann, Nucl. Phys. A325, 216 (1979).

67. P.O. Tjøm, I. Espe, G.B. Hagemann, B. Herskind, and D.L. Hillis, Phys. Lett. 72B, 439 (1978).

68. H.J. Körner, D.L. Hillis, C.P. Roulet, P. Aguer, C. Ellegaard, D.B. Fossan, D. Habs, M. Neiman, F.S. Stephens, and R.M. Diamond, Phys. Rev. Lett. 43, 490 (1979).

69. G.B. Hagemann, Proc. Symp. on High-Spin Phenomena in Nuclei, ANL/PHY-79-4, 1979, Argonne, Ill.

70. O. Andersen, J.D. Garrett, G.B. Hagemann, B. Herskind, D.L. Hillis, and L.L. Riedinger, Phys. Rev. Lett. 43, 687 (1979).

71. M.A. Deleplanque, F.S. Stephens, O. Andersen, J.D. Garrett, B. Herskind, R.M. Diamond, C. Ellegaard, D.B. Fossan, D.L. Hillis, H. Kluge, M. Neiman, C.P. Roulet, S. Shih, and R.S. Simon, Phys. Rev. Lett. 45, 172 (1980).

Figure Captions

Fig. 1. Ground-band γ-ray transitions in ^{174}Yb Coulomb-excited by ^{136}Xe ions scattered at $80^\circ \leq \theta \leq 100^\circ$ into annular detector. Ge counter is also in coincidence with one of two 7.6 x 7.6 cm NaI counters placed at $\pm 90^\circ$ (ref. 2).

Fig. 2. Ground-band γ-ray transitions in ^{238}U Coulomb-excited by ^{208}Pb ions. The two nuclei are scattered into two gas avalanche detectors in coincidence with Ge detector. The spectrum is Doppler-shift corrected (ref. 3).

Fig. 3. Ratios of ground-band B(E2) values for ^{232}Th to those of a rigid rotor (ref. 4).

The dots are ratios of the experimental level energies to those of a rigid rotor.

Fig. 4. A plot of energy <u>vs</u> I for the ground-band rotational levels in ^{164}Yb. The insert shows the same data in the type of plot generally used to show backbending behavior.

Fig. 5. Typical backbending plots for even-even nuclei in the rare-earth region. The plot is of $2\mathcal{J}/\hbar^2 \approx (4I - 2)/E_\gamma(I)$ <u>vs</u> $(\hbar\omega)^2 \approx (E_\gamma(I)/2)^2$.

Fig. 6. Energy levels of ^{164}Er.

Fig. 7. Plot of the level excitation energies for various bands in ^{164}Er from (a) experiment and (b) the rotation-alignment model. The solid circles correspond to even-spin states and the open circles to odd-spin states (ref. 13).

Fig. 8. Plot of $2\mathcal{J}/\hbar^2$ vs $(\hbar\omega)^2$ for members of the ground-state band, γ-vibrational band and aligned bands in ^{164}Er. The open circles on the ground-state band and even-yrast aligned band are corrections for a 45 keV interaction matrix element. The energies of the 10^+_γ and 12^+_γ states were adjusted in accordance with this interaction strength. The circles represent even-spin and the squares odd-spin states (ref. 13).

Fig. 9. Conventional backbending plots for ^{156,158}Er, and for the decoupled band in ^{157}Er. The following expression has been used: $2\mathcal{J}/\hbar^2 = (4I' - 2)/(E_I - E_{I-2})$, where $I' = I$ for the even-even nuclei and $I' = I - j$ for the decoupled band in the odd-mass nucleus (ref. 16).

Fig. 10. A comparison of backbending in ^{157,159,161}Ho with their even-even neighbors. The even-even curves are the usual ones of this type, and the odd-mass bands are treated as described in Fig. 9 (ref. 17).

Fig. 11. Coincidence spectra and highest observed rotational levels of ^{158}Er (ref. 18).

Fig. 12. Backbending plot for ^{158}Er showing the first backbend at $(\hbar\omega)^2 \approx 0.08$ and the second backbend (upbend) at $(\hbar\omega)^2 \approx 0.18$.

Fig. 13. Energy levels as a function of rotational frequency for protons in a prolate nucleus having $\varepsilon = 0.2$ and mass number 165 as calculated by Andersson, et al.[24] The solid and dashed lines correspond to states having different symmetry with respect to $e^{i\pi j_x}$ (different "signatures").

Fig. 14. Cranking model calculations of energy in the rotating frame, $e'(\omega)$ vs ω for neutrons around N = 90. The levels marked A, B, C, and D are components of the $i_{13/2}$ orbital, while those labelled E, F. G, and H have negative parity (N = 5 shell). The different types of lines refer to different signatures of the levels. The figure is from Riedinger et al.[19]

Fig. 15. Plot of alignment, i, vs ω for bands in ^{160}Yb and ^{161}Yb. The proposed labeling of the bands is according to the nomenclature on Fig. 14. Taken from Riedinger et al.[19]

Fig. 16. Angular momentum at which fission barrier becomes zero (solid line) or 8 MeV (dashed line) as a function of mass number (for nuclei along the valley of stability). The stable shape is oblate below ℓ_I and triaxial between ℓ_I and ℓ_{II} (ref. 31).

Fig. 17. Plot of ratio of ellipsoidal moment of inertia to that of a rigid sphere vs γ for two values of the deformation parameter, $\epsilon = 0.3$ and $\epsilon = 0.6$. The right-hand scale gives the difference in rotational energy in MeV for a nucleus with A = 160 and I = 60. The dots give the difference in total liquid-drop energy (rotation + surface + Coulomb) for the nucleus.

Fig. 18. Typical γ-ray deexcitation pathways to the ground state. The statistical transitions are the vertical arrows which lower the temperature of the system, whereas the yrast-like transitions are roughly parallel to the yrast line and remove the angular momentum of the system.

Fig. 19. Level scheme for ^{152}Dy (ref. 37).

Fig. 20. Plot of energy vs I(I + 1) for yrast levels of ^{152}Dy assuming I = 17 for the 60 ns isomer. For I > 14 the data lie close to a straight line with slope corresponding to $2\mathcal{J}/\hbar^2 = 142$ MeV^{-1} (ref. 35).

Fig. 21. Plot of energy vs I^2 for the yrast levels of nuclei with the indicated neutron number as calculated with a spherical Nilsson potential [L.G. Moretto, unpublished work (1979)].

Fig. 22. Sodium iodide pulse-height (squares) and unfolded (black dots) γ-ray spectra (0° + 45° + 90°) from the reaction ^{126}Te(^{40}Ar,4n)^{162}Yb at 181 MeV. The larger dots are averaged over five channels. At the top is the 0°/90° ratio for the unfolded spectra. At the bottom are schematic unfolded spectra for the same case (solid line) and for ^{80}Se(^{86}Kr,4n)^{162}Yb at 331 MeV (dotted line), ^{126}Te(^{40}Ar,4n)^{162}Yb at 157 MeV (longer dashed line), and ^{150}Sm(^{16}O,4n)^{162}Yb at 87 MeV (shorter dashed line) (ref. 43).

Fig. 23. Observed (left) and calculated (right) multiplicity spectra vs E_γ for the ^{124}Sn + ^{40}Ar system at the indicated bombarding energies. One NaI γ-ray spectrum is also shown (ref. 58).

Fig. 24. Plots of multiplicity vs γ-ray transition energy for the systems (a) ^{82}Se + ^{40}Ar and (b) ^{100}Mo + ^{40}Ar for the indicated bombarding energies. One NaI γ-ray spectrum is also shown for each system (ref. 58).

Fig. 25. (a) Spectra at 0° for $^{124}Sn + ^{40}Ar$ system (dashed line) and $^{119}Sn + ^{40}Ar$ system (solid line) in four-fold coincidence with a multiplicity filter. (b) Spectra for ^{154}Er (thick line) and ^{155}Er (dot-dashed line). (c) Multiplicity spectra for the $^{124}Sn + ^{40}Ar$ system (open squares) and the $^{119}Sn + ^{40}Ar$ system (filled squares) (ref. 59).

Fig. 26. Plot of $2\mathcal{J}/\hbar^2$ vs $(\hbar\omega)^2$ for ^{162}Yb. The small dots are the known discrete transitions, and the open circles are the known transitions in the isotone ^{160}Er. The large dots connected by a solid line are values in ^{162}Yb derived by the integral method from the 181 MeV ^{40}Ar spectrum for E_γ between 0.7 and 1 MeV, and the diamonds come from the differential method applied to the same data. The square, triangles, and circle represent values for the moment of inertia derived from the yrast bump edge for 87 MeV ^{16}O, 157 MeV ^{40}Ar, 331 MeV ^{86}Kr, and 181 MeV ^{40}Ar reactions, respectively. The horizontal dashed line corresponds to a rigid diffuse sphere with A=162 (ref. 43).

Fig. 27. Plot of calculated excitation energy vs spin space for $^{124}Sn(^{40}Ar,xn)^{164-x}Er$. Slices of the excitation energy, shown as dashed lines, select particular regions of the space.

Fig. 28. (Top) Spectra from a 7.6 cm x 7.6 cm NaI detector (number of transitions per 200 keV per event) for consecutive ~4 MeV wide slices of the coincident total γ-ray energy spectrum from 185 MeV $^{40}Ar + ^{144}Sn \rightarrow ^{164}Er^*$ observed with a 33 cm x 20 cm sum crystal. (Bottom) The difference in spectra from neighboring slices as indicated in the figure (ref. 68).

Fig. 29. Plot of $2\mathcal{J}/\hbar^2$ vs $(\hbar\omega)^2$ for the compound system $^{164}Er^*$ made by $^{40}Ar + ^{124}Sn$. The solid circles to spin 32 $\hbar$ are the known transitions in ^{158}Er. The symbols without error bars are calculated from the expression $2\mathcal{J}/\hbar^2 = 8/\Delta E_\gamma$ (Eq. 11). The pure liquid-drop prediction is indicated by the dashed line.

Fig. 30. Schematic illustration of the bands in a decay pathway (solid lines) and their envelope (~~dashed~~ dotted line). The plot parameters are somewhat arbitrary but were taken to be $2\mathcal{J}_{coll}/\hbar^2 = 50$ MeV^{-1}, $2\mathcal{J}_{eff}/\hbar^2 = 100$ MeV^{-1}; $j_a = 0$, 10, 18, and 24 $\hbar$ for the bands, in order of increasing energy.

Fig. 31. (a) The evenly spaced (at $8\hbar^2/2\mathcal{J}$) transitions from the state indicated for an idealized rigid rotor. (b) The spectrum observed in counter 2 in coincidence with a gate on the $I \rightarrow I - 2$ transition in counter 1. (c) Same as (b), but there are three rotational bands with slightly different values of $\mathcal{J}$, although all have the same effective value for the $I \rightarrow I - 2$ transition.

Fig. 32. Schematic correlation plot for a rotational nucleus. The dots locate the coincidences for a band with spins up to 14 $\hbar$ and moment of inertia $\mathcal{J}$, and the heavy lines show the effect of bands where $\mathcal{J}$ differs by ±10 percent. The crosses show the location of coincidences in a band with spins 16 to 26 $\hbar$, 11 $\hbar$ of aligned angular momentum, and moment of inertia $\mathcal{J}$. The light lines again show the effect of bands differing in $\mathcal{J}$ by 10 percent.

Fig. 33. Correlation spectrum from the reaction $^{124}Sn(^{40}Ar,xn)^{164-x}Er$ at 185 MeV. The data were taken in Ge(Li) detectors and treated according to Eq. (20). The plot shows contours of equal numbers of correlated events, where the darker regions have more counts according to the scale at the right edge. These data are from ref. 71.

Fig. 34. Correlation array from the reaction $^{130}Te(^{40}Ar,xn)^{170-x}Yb$ at 185 MeV. The data were taken with Ge(Li) detectors, and the resulting array had the background subtraction iterated 16 times (Eq. 21) and was approximately efficiency corrected by multiplying by $E_1 \times E_2$.

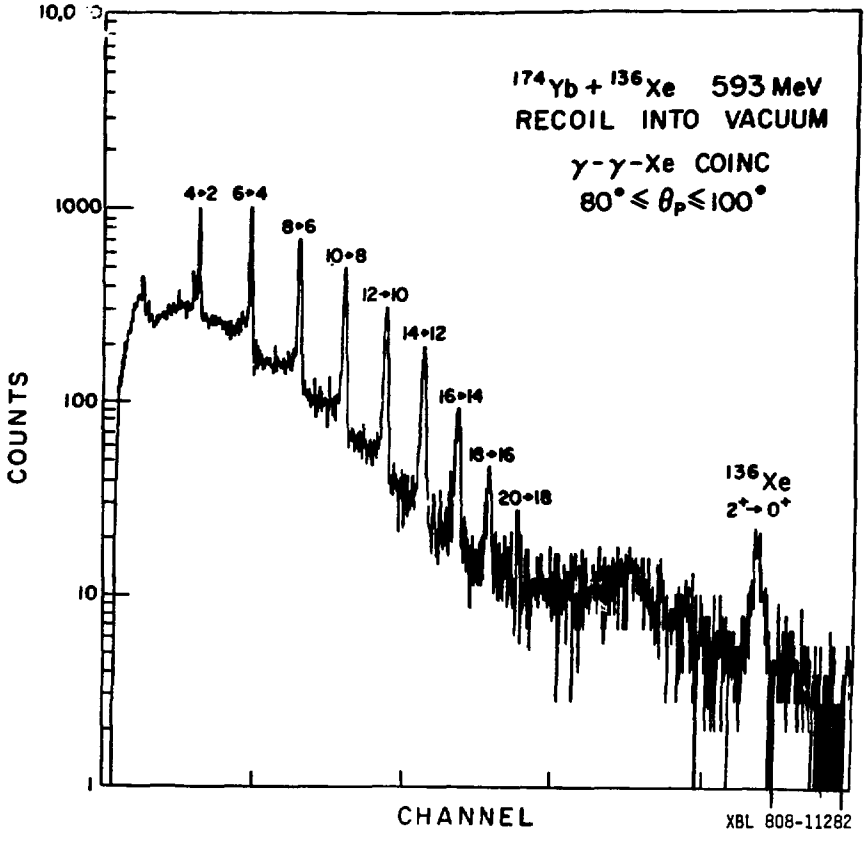
10,000
1000
100
10
1
COUNTS
CHANNEL
^{174}Yb + ^{136}Xe 593 MeV
RECOIL INTO VACUUM
γ-γ-Xe COINC
80° ≤ θp ≤ 100°
4→2
6→4
8→6
10→8
12→10
14→12
16→14
18→16
20→18
^{136}Xe
2+→0+
XBL 808-11282

Fig. 1

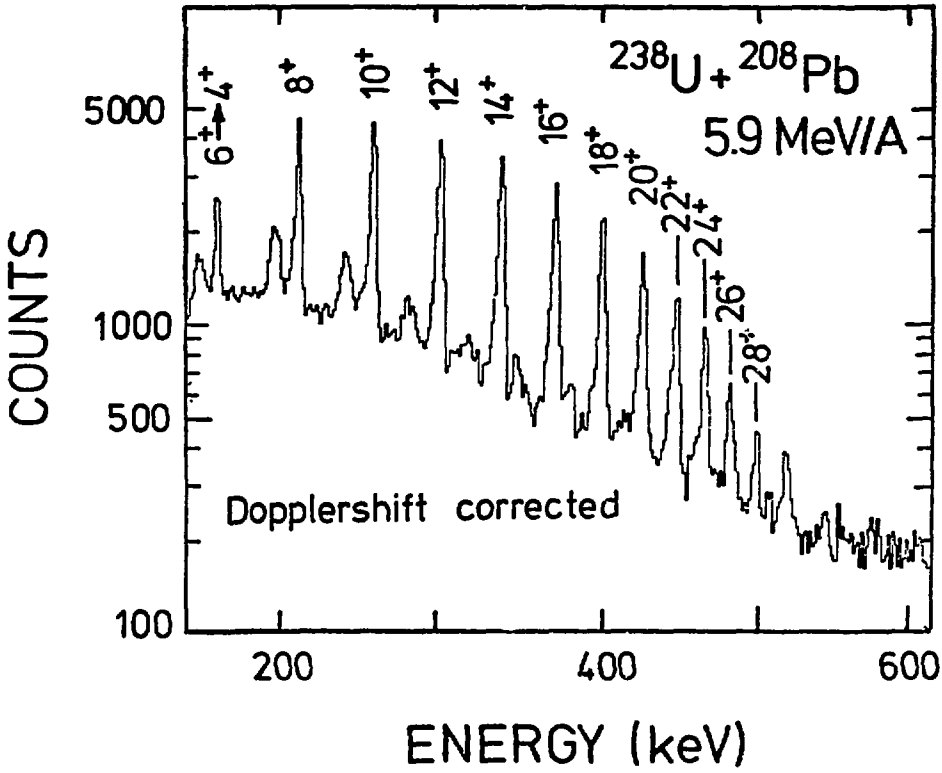

XBL 808-11281

Fig. 2

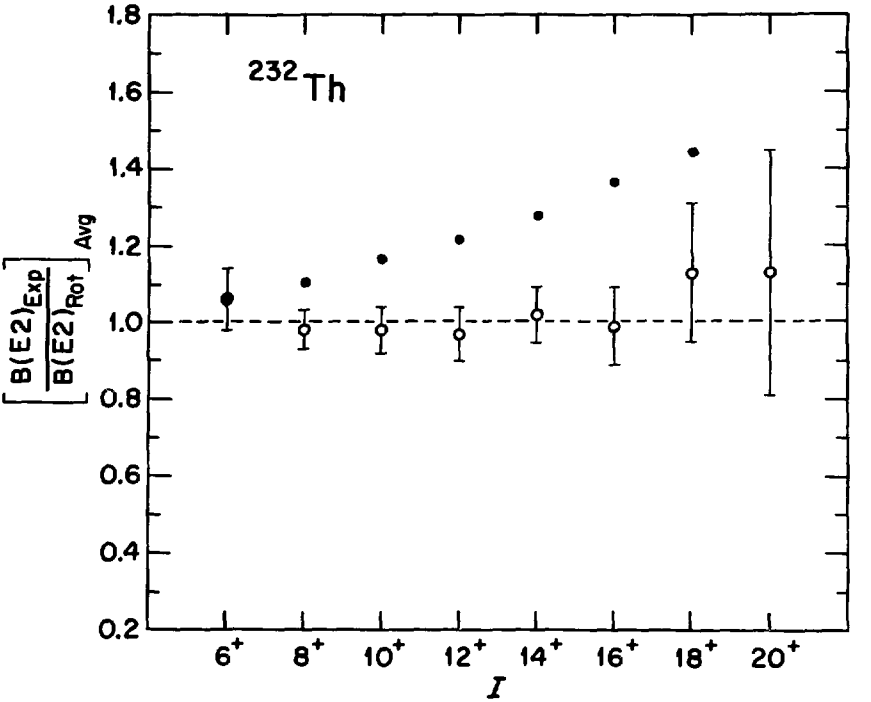

XBL 765-1803 A

Fig. 3

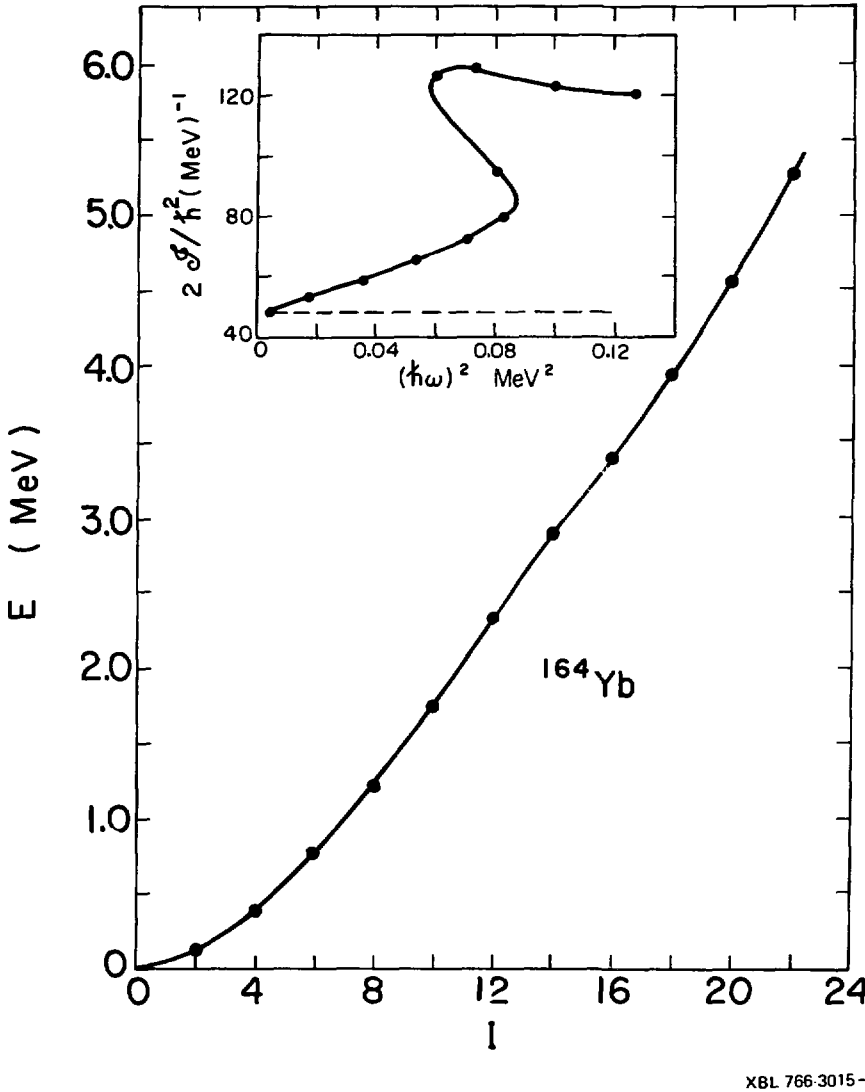

XBL 766-3015-A

Fig. 4

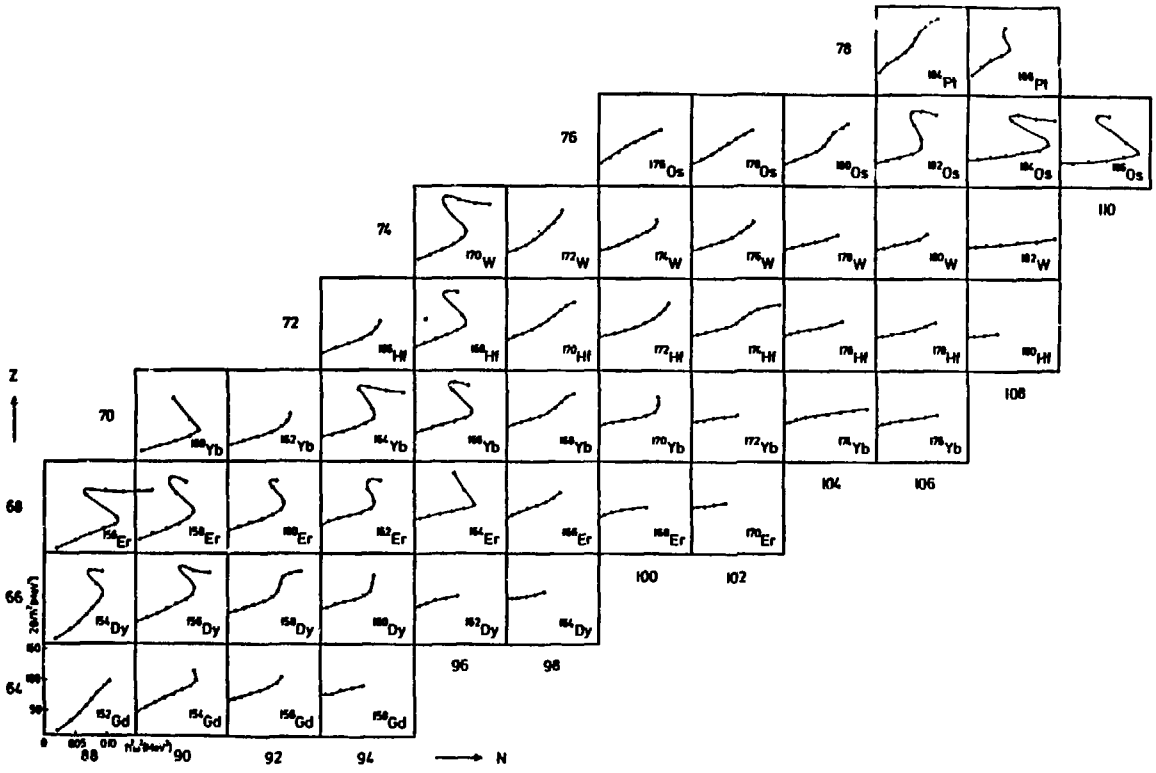

XBL 7811-12899

Fig. 5

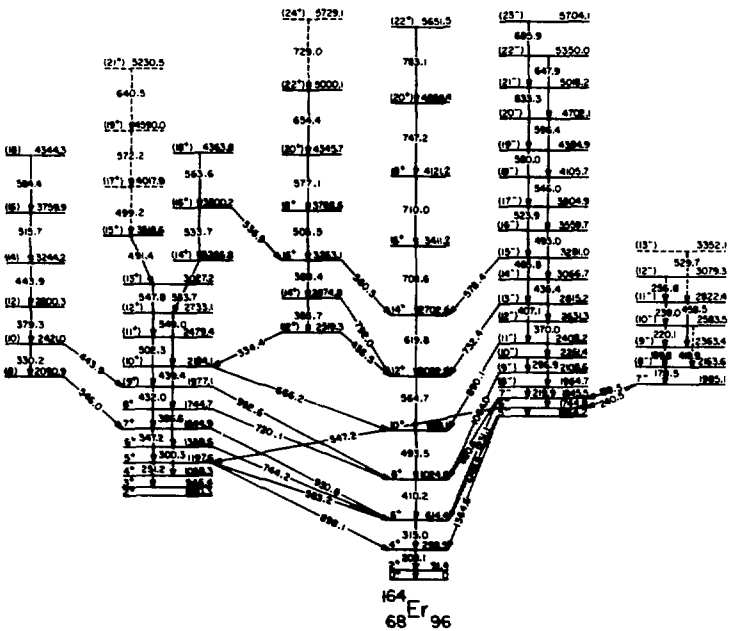

XBL 808-11283

Fig. 6

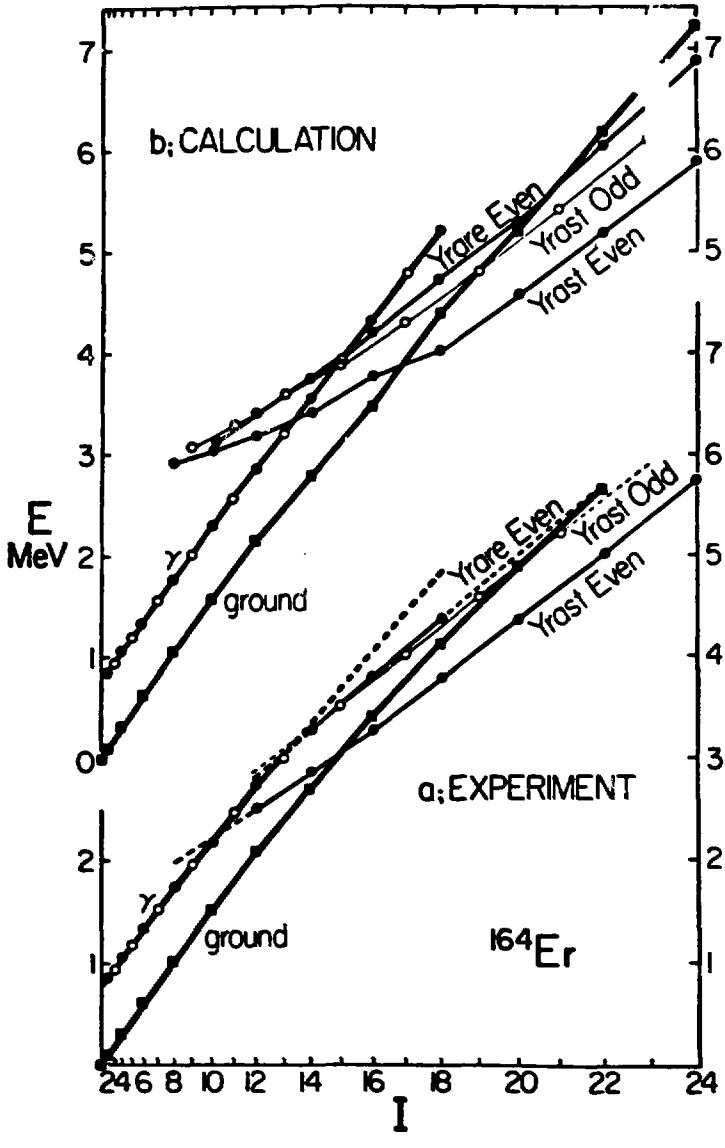

XBL 7811-12920

Fig. 7

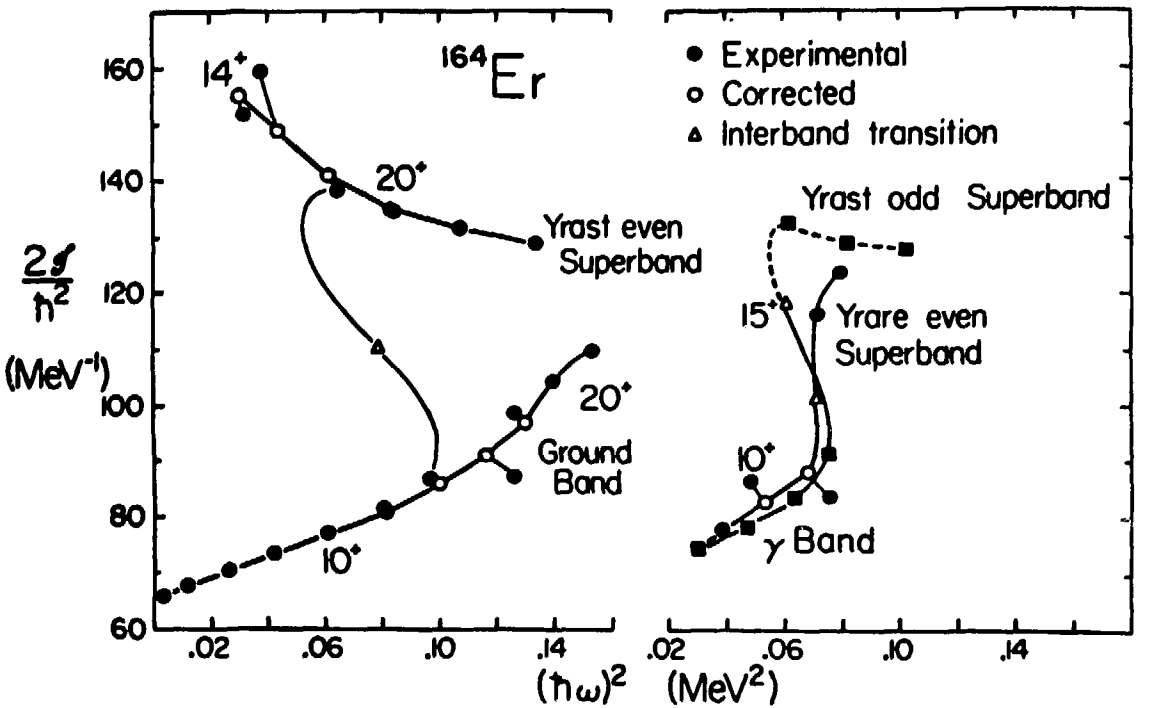

XBL 806-9889

Fig. 8

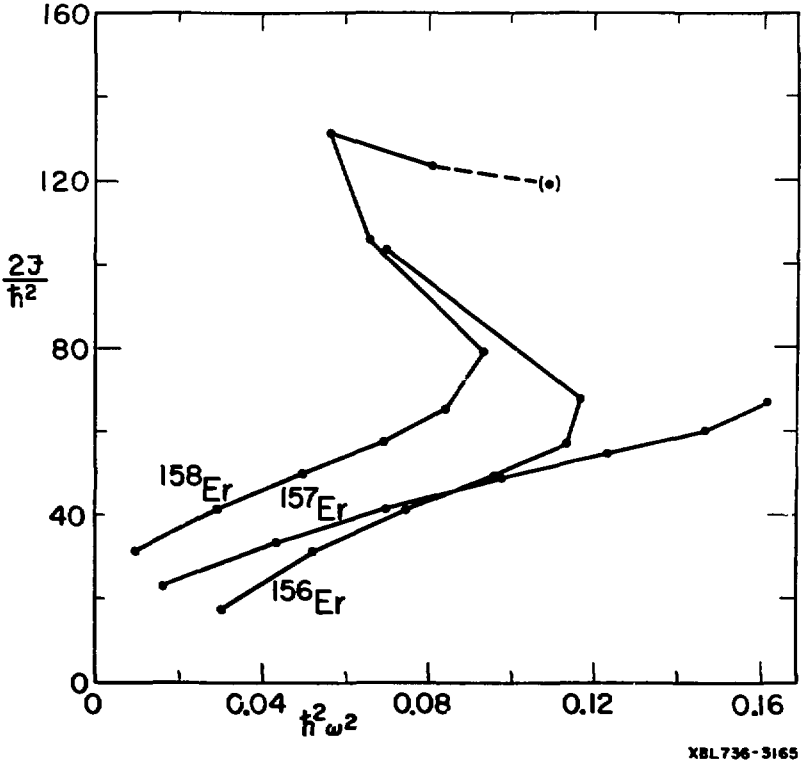
160
120
80
40
0
$\frac{2\mathcal{J}}{\hbar^2}$
(•)
158Er
157Er
156Er
0
0.04
0.08
0.12
0.16
$\hbar^2\omega^2$
XBL736-3165

Fig. 9

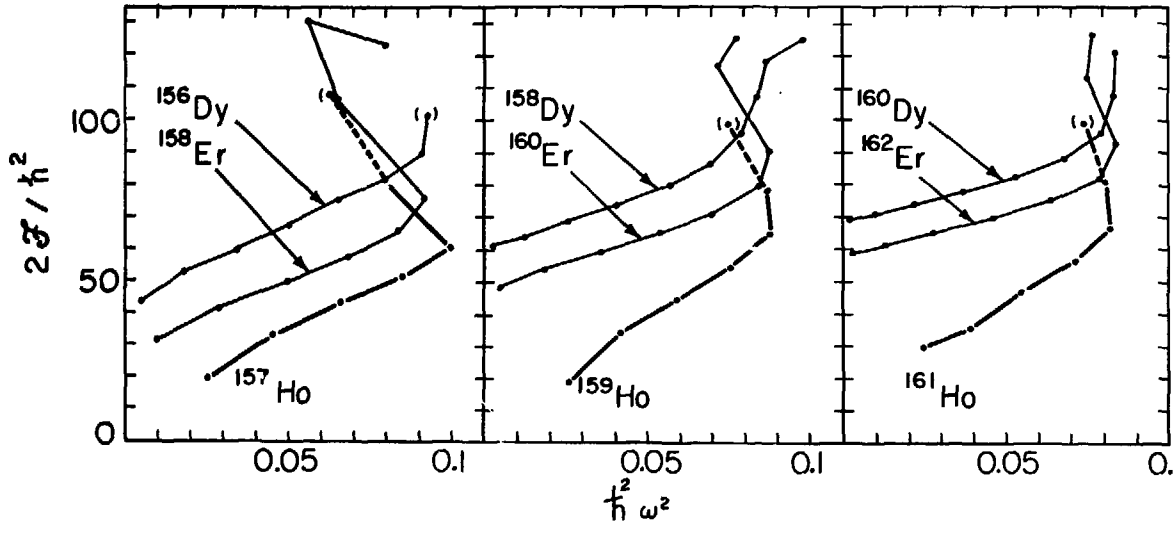

XBL7310-4146

Fig. 10

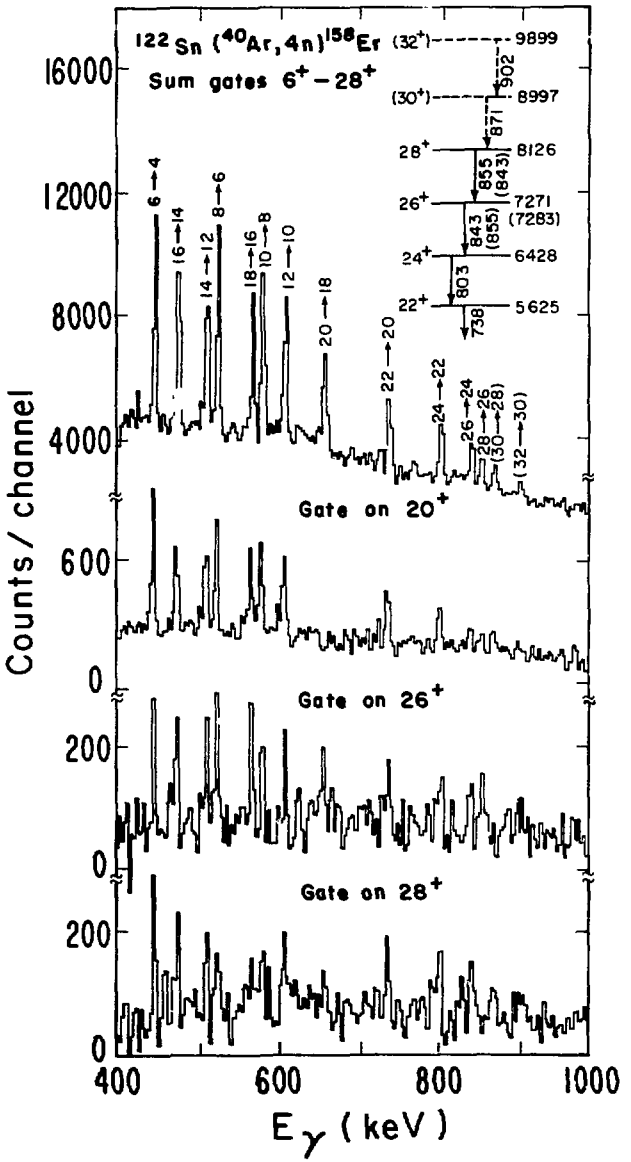

XBL 774-805

Fig. 11

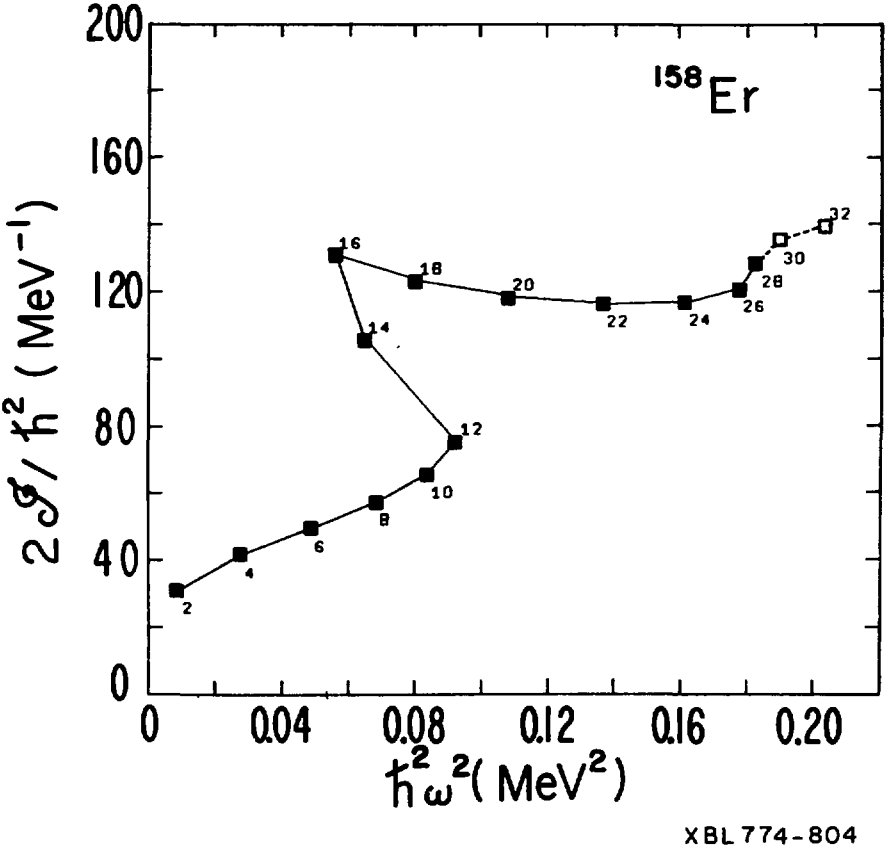
158Er
200
160
120
80
40
0
0
0.04
0.08
0.12
0.16
0.20
2𝒥/ħ² (MeV⁻¹)
ħ²ω² (MeV²)
2
4
6
8
10
12
14
16
18
20
22
24
26
28
30
32
XBL 774-804

Fig. 12

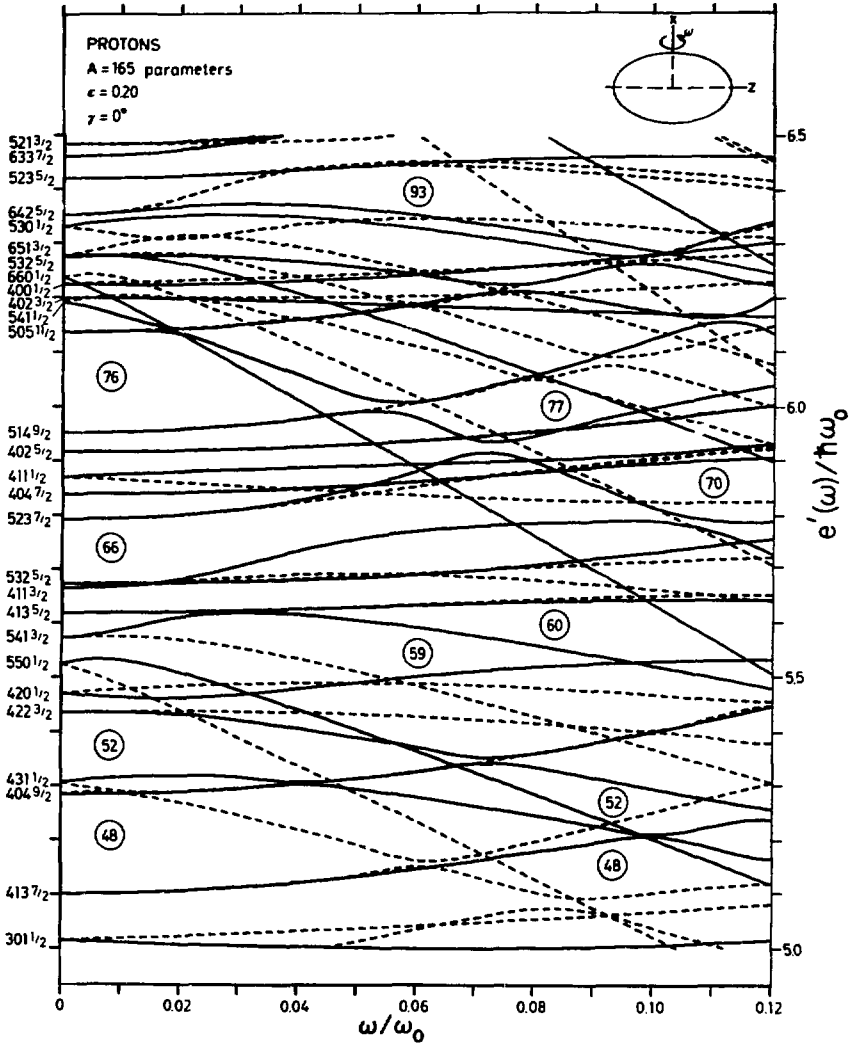

XBL 806-9888

Fig. 13

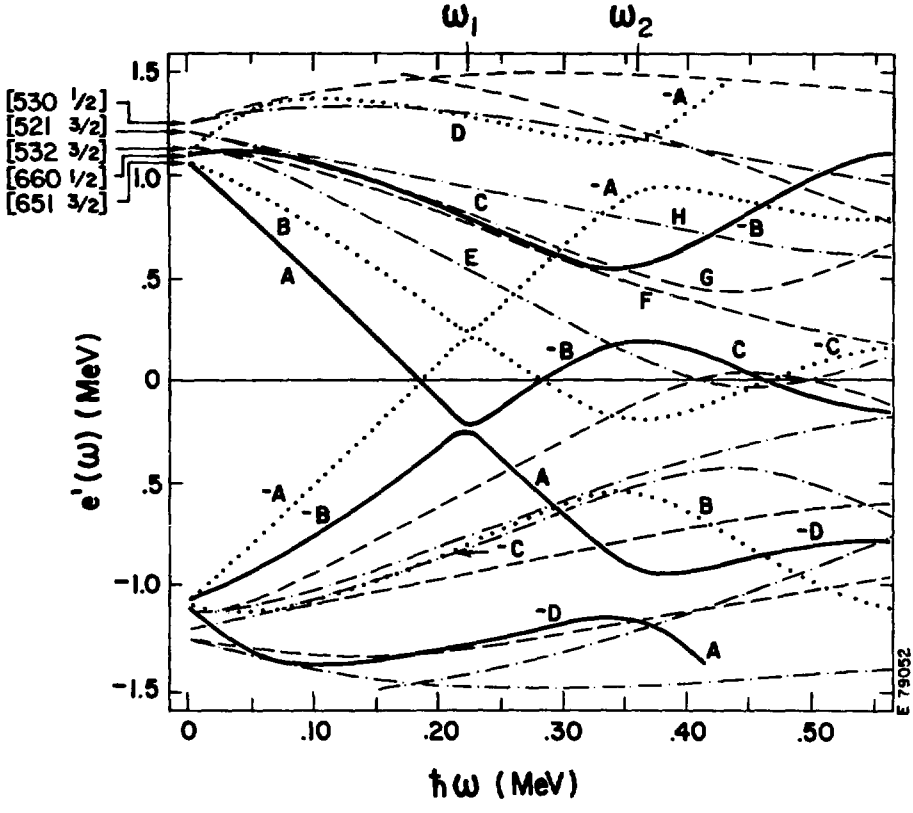

XBL 806-9886

Fig. 14

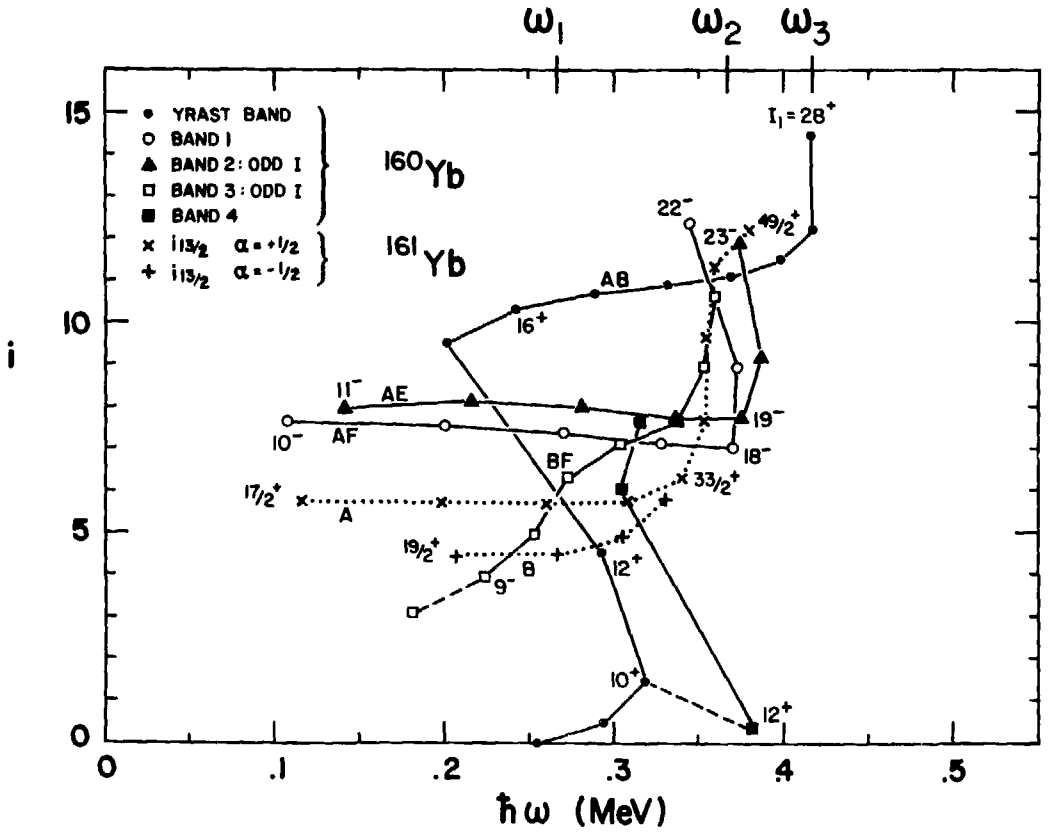

XBL 804-9229

Fig. 15

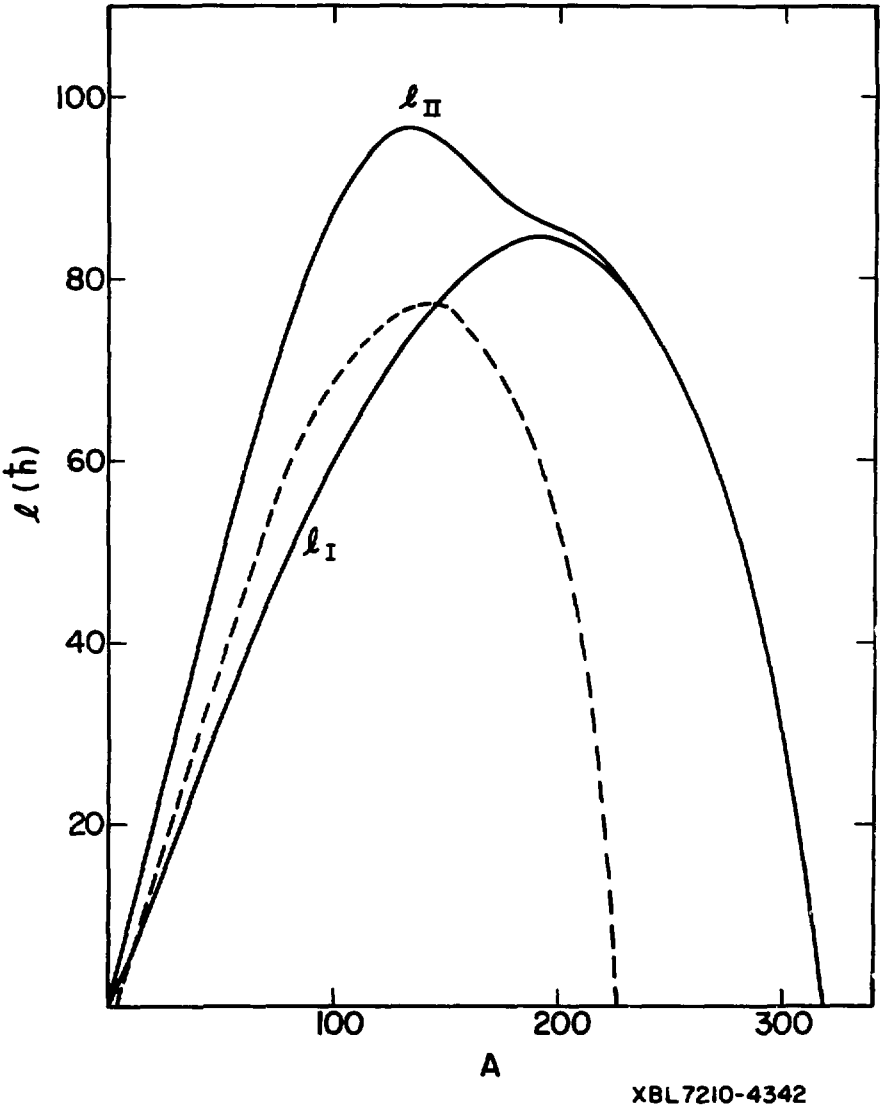

Fig. 16

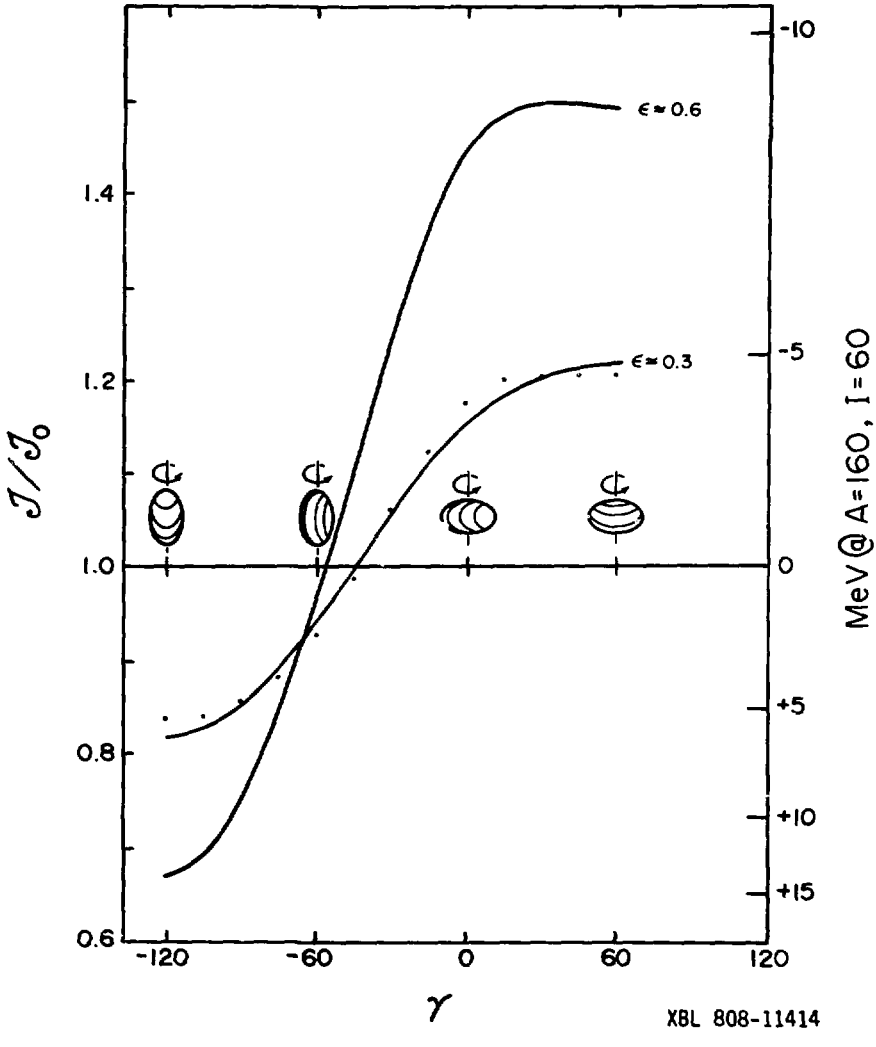
ε≈0.6
ε≈0.3
1.4
1.2
1.0
0.8
0.6
-120
-60
0
60
120
γ
-10
-5
0
+5
+10
+15
MeV @ A=160, I=60
XBL 808-11414

Fig. 17

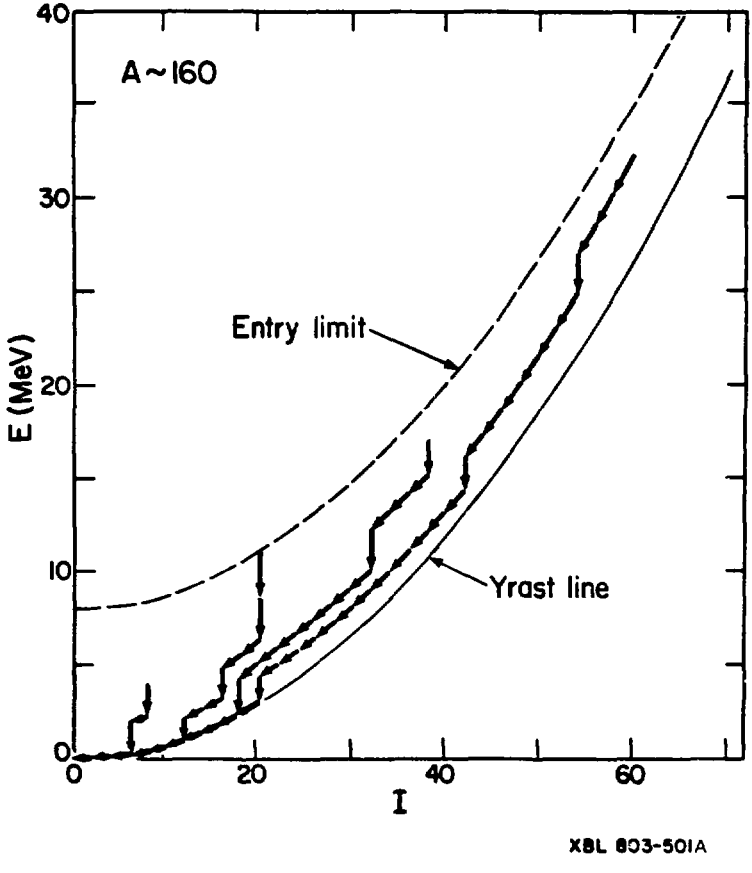
A~160
Entry limit
Yrast line
E (MeV)
I
0
10
20
30
40
0
20
40
60
XBL 803-501A

Fig. 18

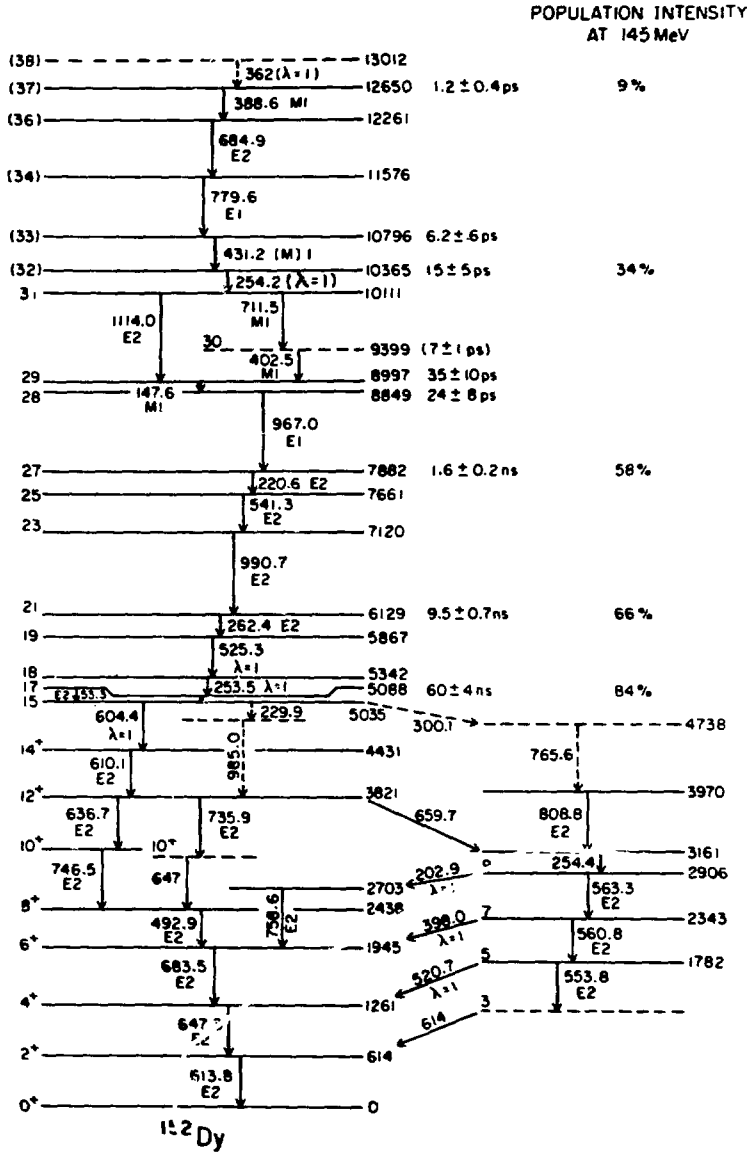
POPULATION INTENSITY
AT 145 MeV
(38)
13012
362(λ=1)
(37)
12650
1.2 ± 0.4 ps
9%
388.6 M1
(36)
12261
684.9
E2
(34)
11576
779.6
E1
(33)
10796
6.2 ± 6 ps
431.2 (M) 1
(32)
10365
15 ± 5 ps
34%
254.2 (λ=1)
31
10111
1114.0
E2
711.5
M1
30
9399
(7 ± 1 ps)
402.5
M1
29
8997
35 ± 10 ps
28
147.6
M1
8849
24 ± 8 ps
967.0
E1
27
7882
1.6 ± 0.2 ns
58%
220.6 E2
25
7661
541.3
E2
23
7120
990.7
E2
21
6129
9.5 ± 0.7 ns
66%
262.4 E2
19
5867
525.3
λ=1
18
5342
17
5088
60 ± 4 ns
84%
253.5 λ=1
15
229.9
5035
300.7
4738
604.4
λ=1
14+
4431
610.1
E2
765.6
12+
3821
3970
636.7
E2
735.9
E2
659.7
808.8
E2
10+
3161
746.5
E2
647
254.4
2906
202.9
λ=1
2703
563.3
E2
8+
2438
492.9
E2
758.6
E2
398.0
λ=1
2343
560.8
E2
6+
1945
683.5
E2
520.7
λ=1
1782
553.8
E2
4+
1261
614
2+
614
613.8
E2
0+
0
152Dy
XBL 806-9887

Fig. 19

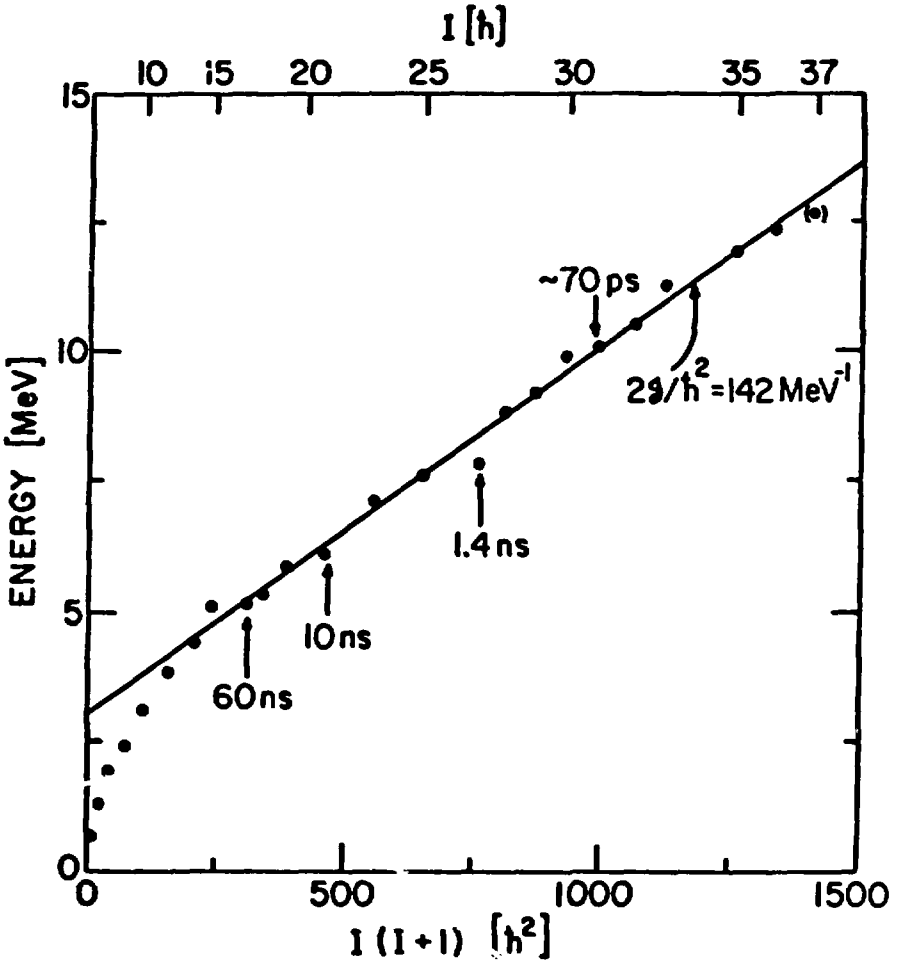

XBL 788-10388

Fig. 20

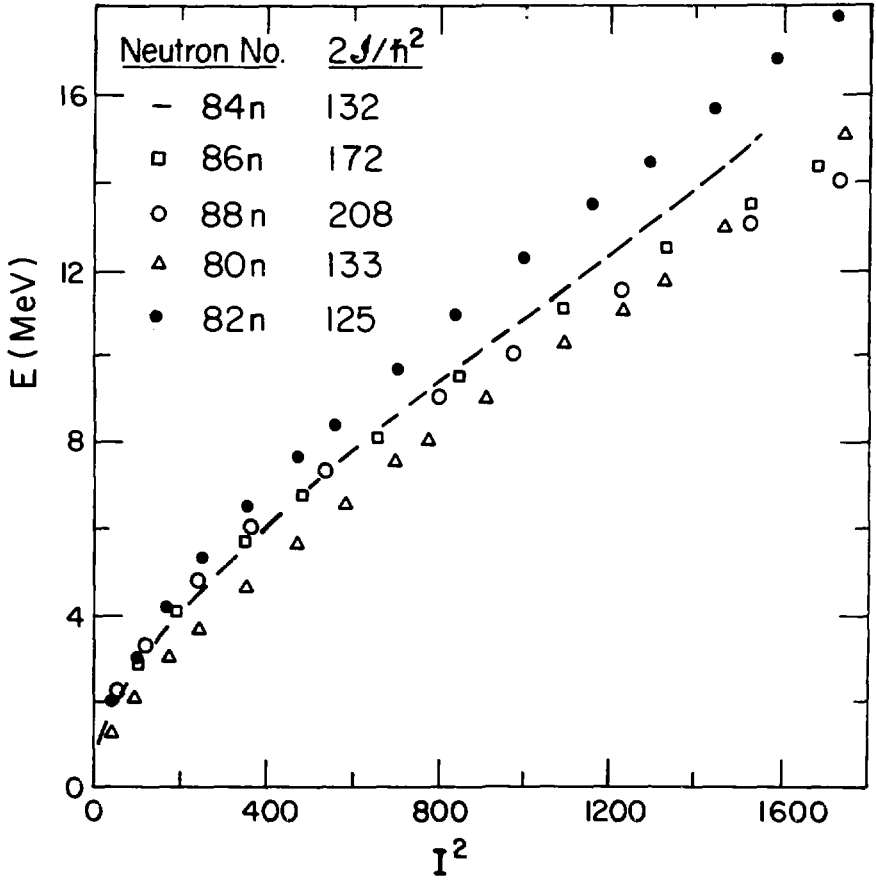

XBL 803-524

Fig. 21

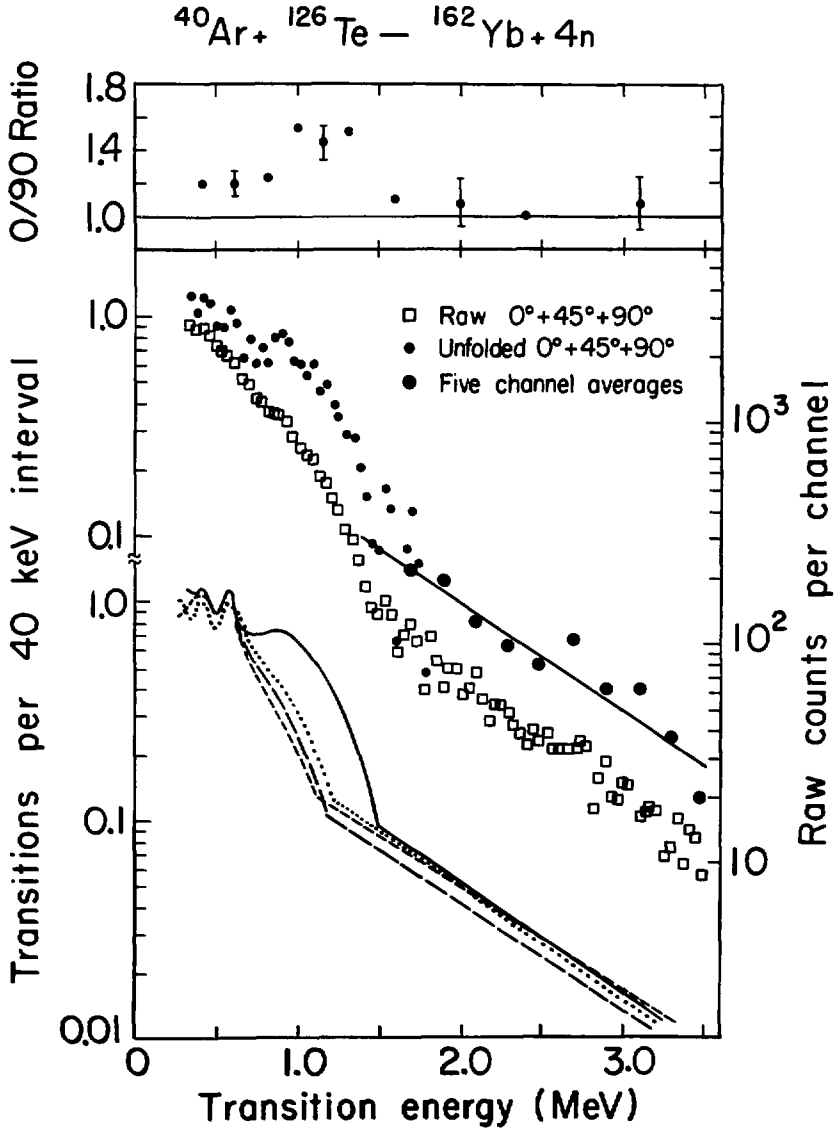

XBL 771-162

Fig. 22

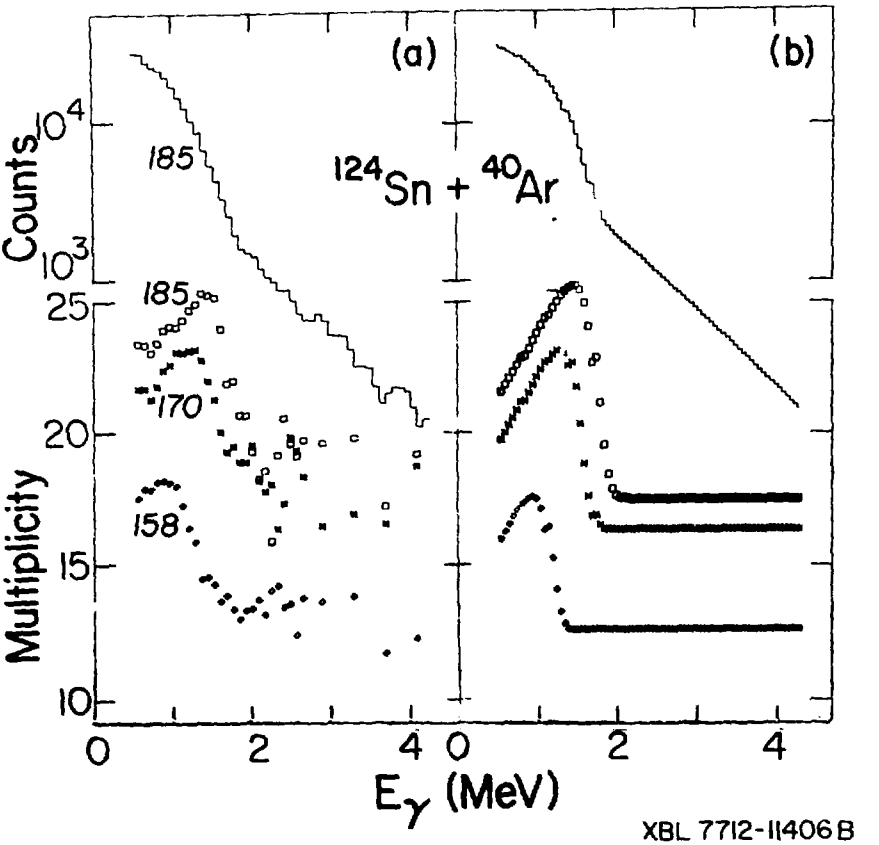
(a)
(b)
Counts
10^4
10^3
185
^{124}Sn + ^{40}Ar
Multiplicity
25
20
15
10
185
170
158
0
2
4
0
2
4
E_γ (MeV)
XBL 7712-11406B

Fig. 23

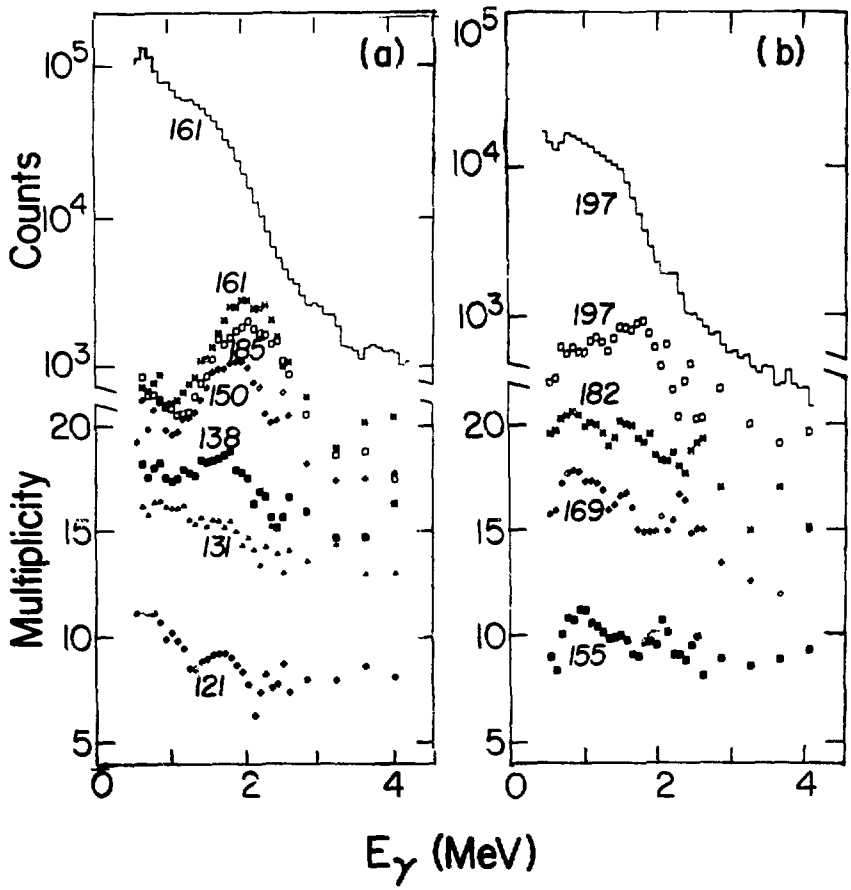

XBL803-529

Fig. 24

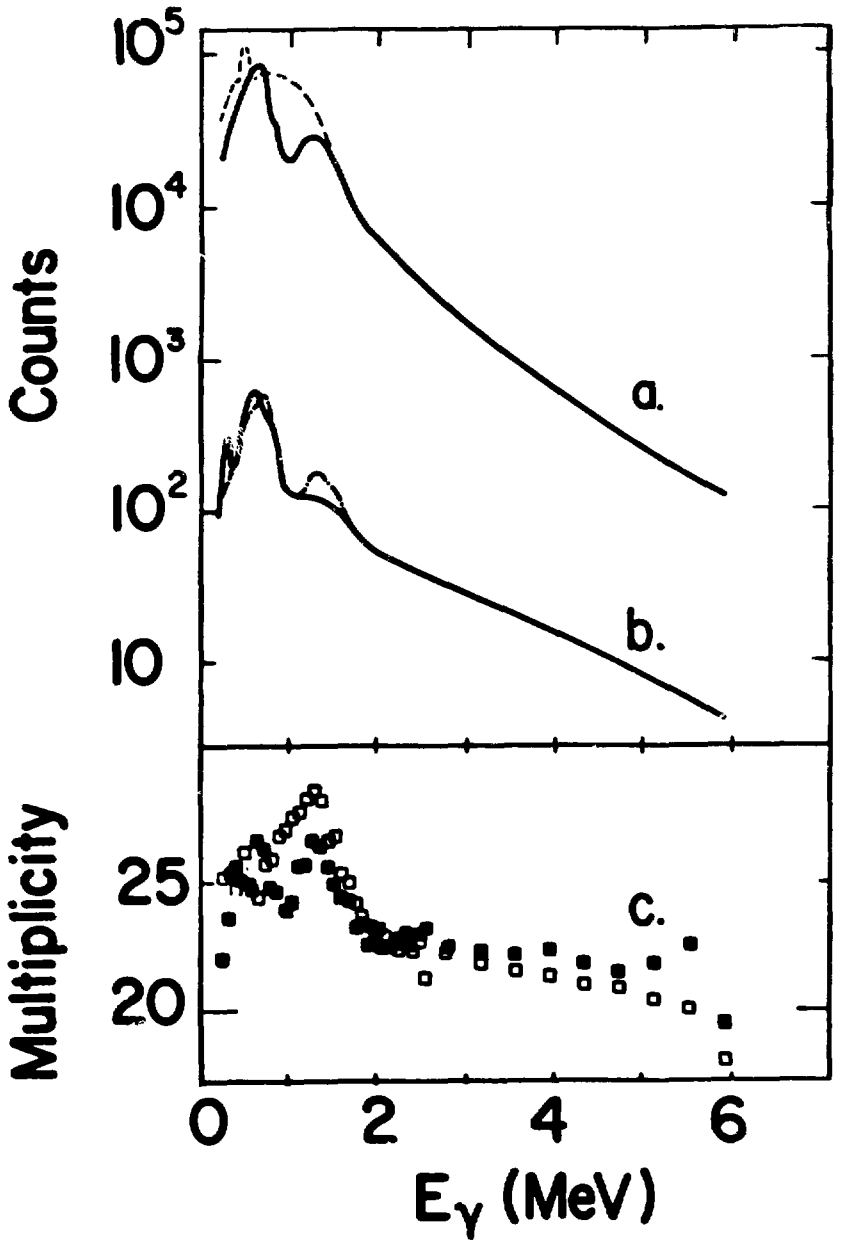

XBL 7911-12915B

Fig. 25

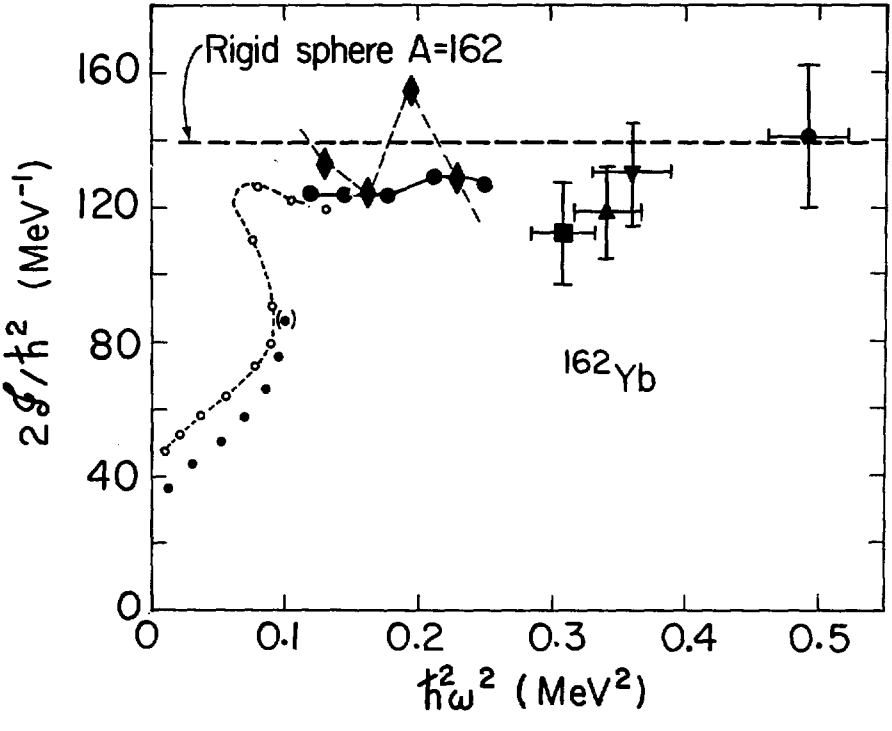

XBL 771-161

Fig. 26

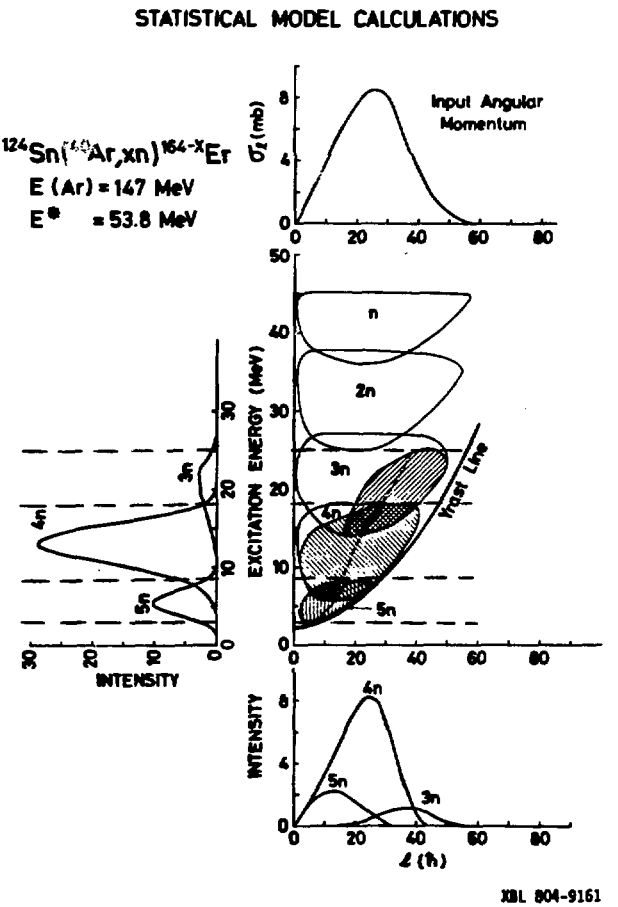
STATISTICAL MODEL CALCULATIONS
124Sn(40Ar,xn)164-xEr
E (Ar) = 147 MeV
E* = 53.8 MeV
Input Angular Momentum
σℓ (mb)
EXCITATION ENERGY (MeV)
INTENSITY
ℓ (ħ)
n
2n
3n
4n
5n
Yrast Line
XBL 804-9161

Fig. 27

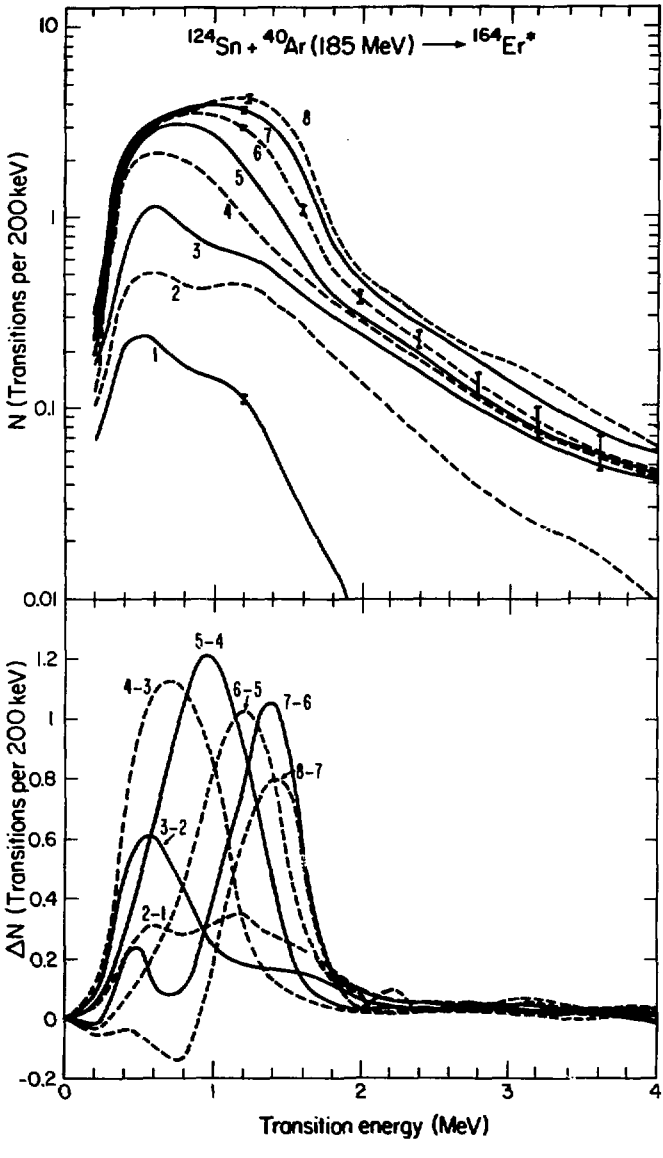

XBL 792-645A

Fig. 28

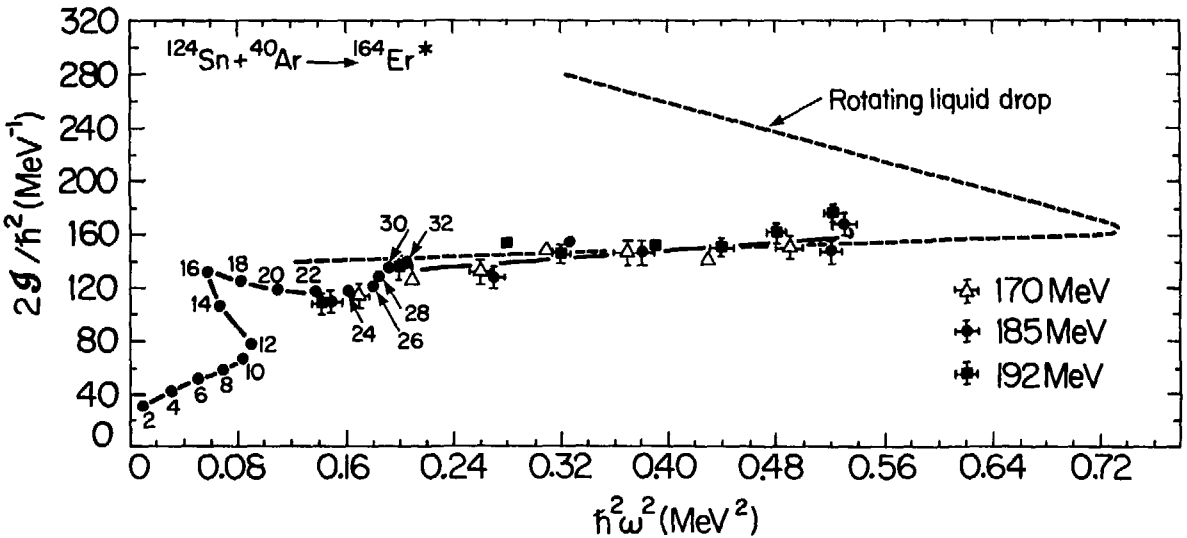

XBL 798-2729

Fig. 29

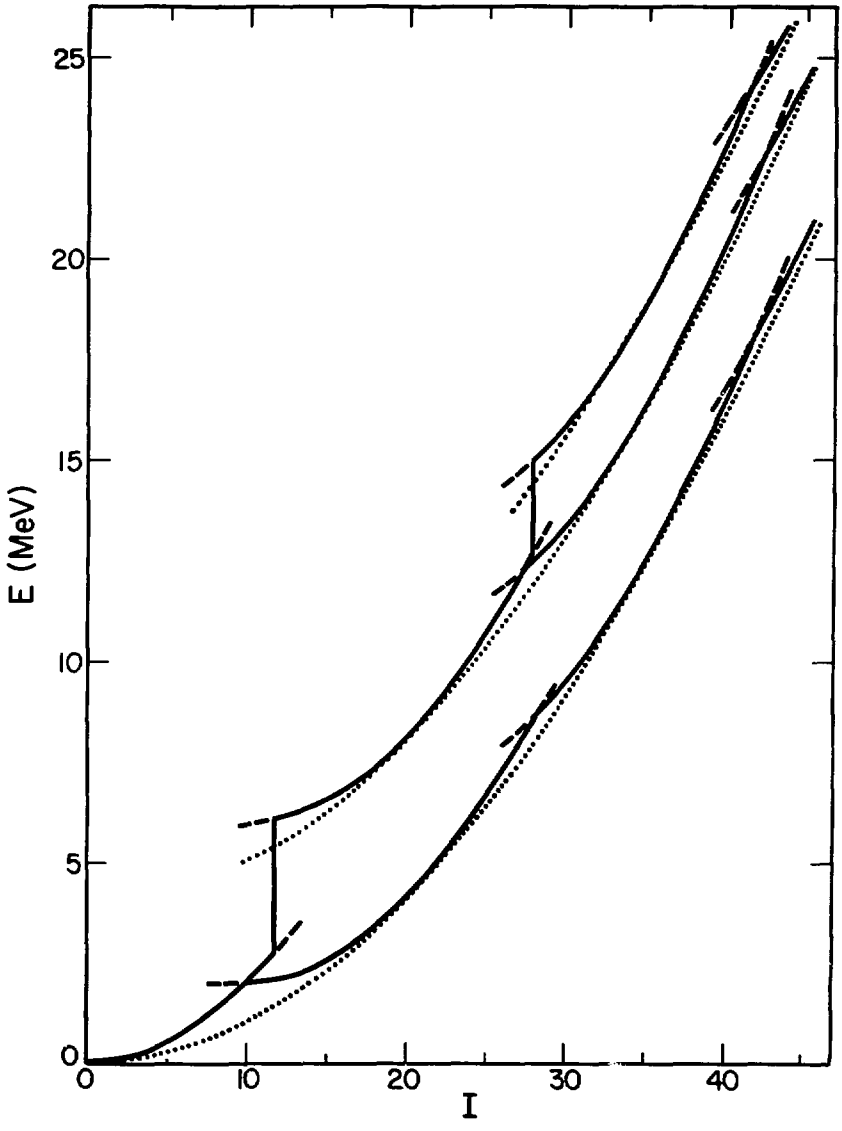

XBL 803-502

Fig. 30

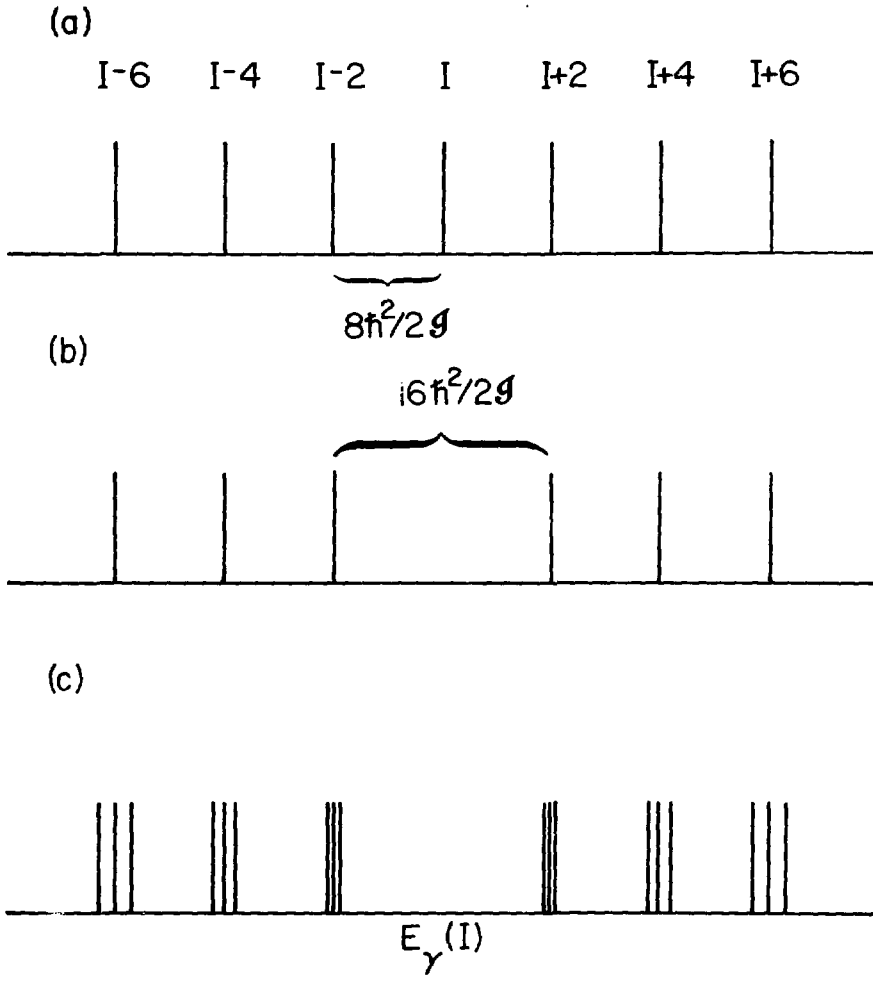

XBL 798-2732

Fig. 31

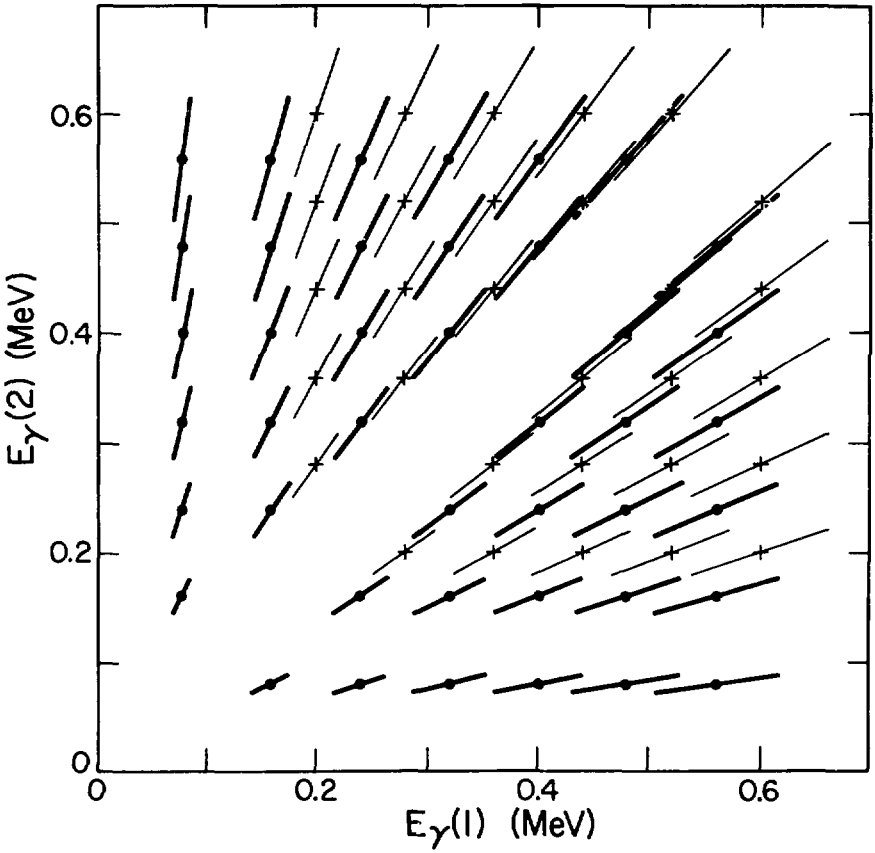

XBL 803-482

Fig. 32

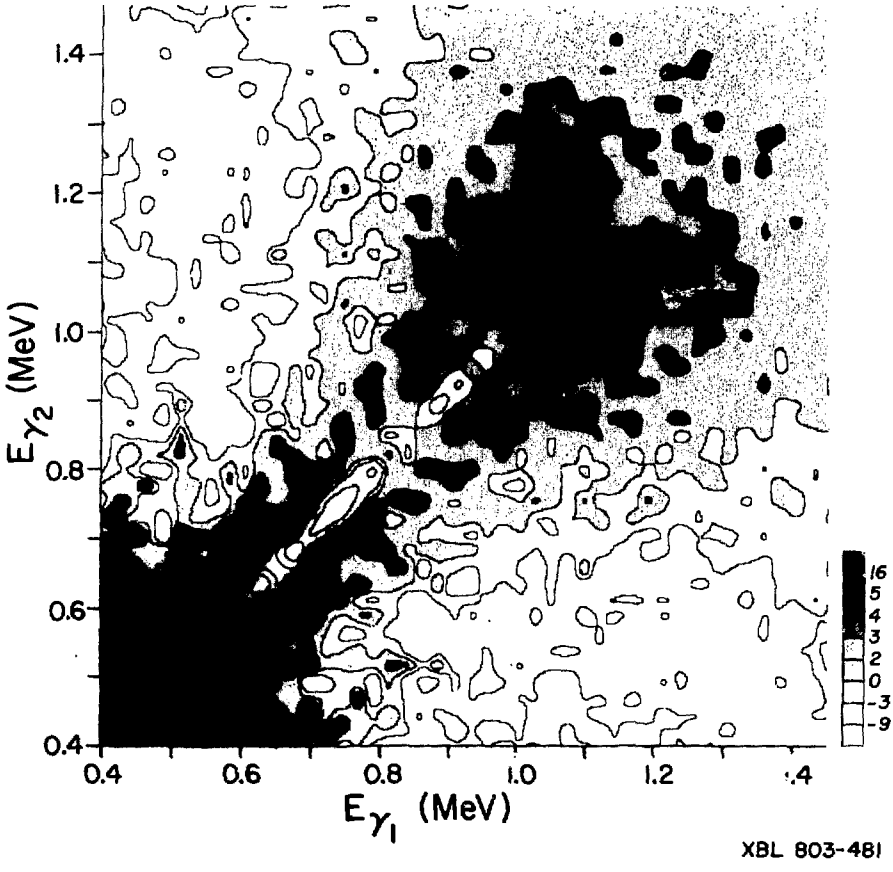
1.4
1.2
1.0
0.8
0.6
0.4
E_{γ_2} (MeV)
0.4
0.6
0.8
1.0
1.2
1.4
E_{γ_1} (MeV)
16
5
4
3
2
0
-3
-9
XBL 803-481

Fig. 33

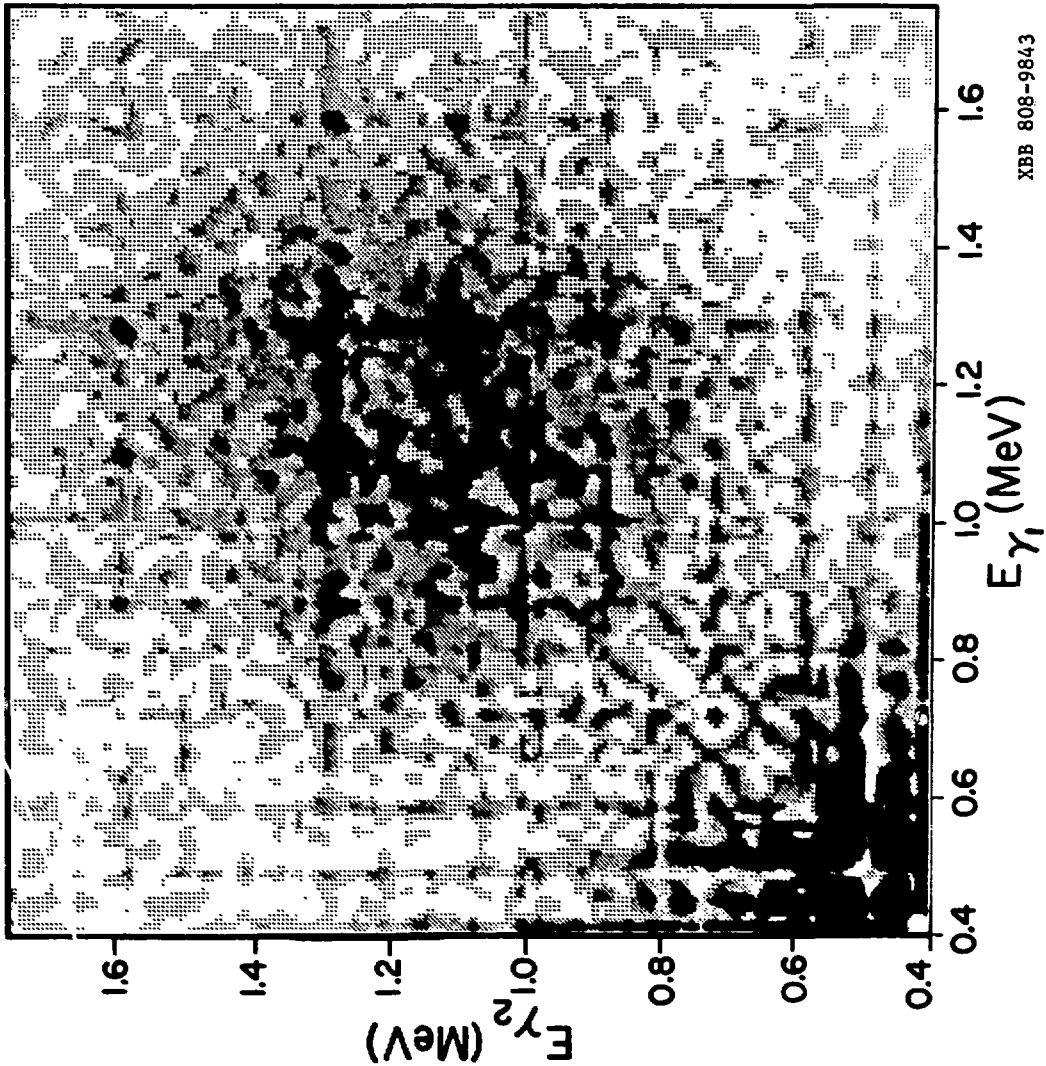
1.6
1.4
1.2
1.0
0.8
0.6
0.4
E_{γ_2} (MeV)
0.4
0.6
0.8
1.0
1.2
1.4
1.6
E_{γ_1} (MeV)
XBB 808-9843

Fig. 34